J. Fluid Mech. (1996), *vol.* 311, *pp.* 1–36

Stability of confined swirling flow with and without vortex breakdown

By A. Yu. GELFGAT, P. Z. BAR-YOSEPH† AND A. SOLAN

Computational Mechanics Laboratory, Faculty of Mechanical Engineering, Technion – Israel Institute of Technology, Haifa 32000, Israel; *e-mail* merbygr@cmlp.technion.ac.il

(Received 10 July 1994 and in revised form 9 October 1995)

A numerical investigation of steady states, their stability, onset of oscillatory instability, and slightly supercritical unsteady regimes of an axisymmetric swirling flow of a Newtonian incompressible fluid in a closed circular cylinder with a rotating lid is presented for aspect ratio (height/radius) $1 \leqslant \gamma \leqslant 3.5$. Various criteria for the appearance of vortex breakdown are discussed. It is shown that vortex breakdown takes place in this system not as a result of instability but as a continuous evolution of the stationary meridional flow with increasing Reynolds number. The dependence of the critical Reynolds number Re_{cr} and frequency of oscillations ω_{cr} on the aspect ratio of the cylinder γ is obtained. It is found that the neutral curve $Re_{cr}(\gamma)$ and the curve $\omega_{cr}(\gamma)$ consist of three successive continuous segments corresponding to different modes of the dominant perturbation. The calculated critical parameters are in good agreement with the available experimental and numerical data for $\gamma < 3$. It is shown that the onset of the oscillatory instability does not depend on the existence of a separation bubble in the subcritical steady state. By means of a weakly nonlinear analysis it is shown that the axisymmetric oscillatory instability sets in as a result of a supercritical Hopf bifurcation for each segment of the neutral curve. A weakly nonlinear asymptotic approximation of slightly supercritical flows is carried out. The results of the weakly nonlinear analysis are verified by direct numerical solution of the unsteady Navier–Stokes equation using the finite volume method. The analysis of the supercritical flow field for aspect ratio less than 1.75, for which no steady vortex breakdown is found, shows the existence of an oscillatory vortex breakdown which develops as a result of the oscillatory instability.

1. Introduction

Vortex breakdown in a closed circular cylinder with a rotating lid was discovered experimentally by Vogel (1975) and since that time it has been a subject of intensive experimental and theoretical investigation. The phenomenon takes place as a sudden appearance of one or more separation vortex bubbles at the axis of the cylinder with stagnation points upstream and downstream of the bubble. Later an analogous phenomenon was found in the polar region between concentric rotating spheres (Bar-Yoseph, Roesner & Solan 1992; Arkadyev *et al.* 1993; Bar-Yoseph 1994; Bar-Yoseph & Kryzhanovski 1995). The importance of the vortex breakdown of swirling flows for many applications (see reviews by Escudier 1988, Hopfinger & Linden 1990, and Delery 1994) led to wide interest in this particular problem, which can be investigated relatively easily both experimentally and numerically.

A parametric study of the appearance and disappearance of the separation bubbles

† Author to whom correspondence should be addressed.

in this system was done experimentally by Escudier (1984), who presented the corresponding flow-regime diagram in coordinates of the two control parameters – the Reynolds number and the aspect ratio (height/radius) of the cylinder. An important conclusion of the experimental investigation was that the flow remains axisymmetric at least until the onset of the oscillatory instability. The resulting oscillatory flows observed in the experiment for cylinders with aspect ratio less than three also remained axisymmetric. In cases of larger aspect ratios a spiral motion of the separation bubble around the axis was detected. However, streaklines observed in experiments may spiral even in cases of completely axisymmetric flow (Neitzel 1988). Hence one cannot be sure that a spiralling streakline observed in an experiment really corresponds to a break of axisymmetry.

Escudier (1984) used the term 'stability boundaries' both for the boundaries of parametric regions where flows with one, two, or three separation bubbles were observed and for the boundary dividing steady and unsteady states of the flow. However, in later works (Lugt & Abboud 1987; Tsitverblit 1993) devoted to the numerical analysis of the problem the instability nature of the vortex breakdown in this system was questioned. None of the numerical investigations (Daube & Sørensen 1989; Sørensen & Daube 1989; Lopez 1990; Brown & Lopez 1990; Lopez & Perry 1992; Daube 1992; Tsitverblit 1993) reported any bifurcational transitions between different steady states of the flow. The numerically calculated steady flows with and without vortex breakdown, as well as the calculated transitions from steady to oscillatory states (Lugt & Abboud 1987; Daube & Sørensen 1989; Lopez 1990; Daube 1992; Tsitverblit 1993, Tsitverblit & Kit 1994; Gelfgat, Bar-Yoseph & Solan 1995), are in good agreement with the experimental results (Vogel 1975; Escudier 1984; Roesner 1990).

The only attempt to use linear stability theory for the analysis of a possible instability that could lead to vortex breakdown in the disk–cylinder system was done by Tsitverblit (1993) who showed that the problem linearized in the vicinity of a stationary solution has no single-zero eigenvalues. This means that there is no monotonic instability corresponding to a transition from one steady state to another. On the basis of a series of numerical experiments, Tsitverblit drew some additional qualitative conclusions about the non-existence of other hypothetic instability phenomena leading to vortex breakdown. This analysis did not eliminate possible instabilities corresponding to complex or multiple-zero eigenvalues of the linearized problem. Hence, the connection between flow instability and vortex breakdown is open to further study.

The main objective of the present work is the numerical analysis of the linear stability of the swirling flow in a cylinder with a rotating lid. The spectrum of the problem, linearized in the vicinity of a stationary solution, is investigated for fixed values of the aspect ratio and continuously increasing Reynolds number. The most unstable modes are described by the eigenfunctions corresponding to the dominant eigenvalue with zero real part. It is shown that the vortex breakdown, as well as transitions from one to two (or more) separation bubbles, do not take place because of an instability, and all the steady states observed in the system belong to one single branch of the stationary solution. On the basis of the results obtained we discuss the definition for the vortex breakdown in this particular case. It is shown that the vortex breakdown may be associated not only with the appearance and disappearance of a separation vortex bubble, but also with the concave shape of the streamlines near the axis of rotation. Since vortex breakdown cannot be interpreted as an instability of the flow, we propose an heuristic explanation of the appearance of the separation vortex bubble.

The numerical investigation of the onset of oscillatory instability shows that the transition from the steady to the oscillatory state of the flow takes place as a result of a Hopf bifurcation and yields the dependence of the critical Reynolds number Re_{cr} and the critical frequency of oscillations ω_{cr} on the aspect ratio γ of the cylinder. It is found that the neutral curve $Re_{cr}(\gamma)$ and the curve $\omega_{cr}(\gamma)$ consist of three successive continuous segments corresponding to different modes of dominant perturbation. It is shown that the onset of the oscillatory instability is not connected with the vortex breakdown. For the aspect ratio changing from one to three the values of the critical Reynolds number obtained are in good agreement with published experimental and numerical results. For larger aspect ratios the calculated critical Reynolds numbers are larger than the values obtained experimentally (Escudier 1984).

A weakly nonlinear analysis of the branching periodic solutions showed that the numerically obtained axisymmetric Hopf bifurcation is supercritical for all values of the aspect ratio which were considered. This leads to the conclusion that for aspect ratio larger than three the experimentally observed threshold from steady to oscillatory flow is connected with an asymmetric instability of the flow. Moreover, it has been shown that an oscillatory vortex bubble exists in the case of aspect ratio less than 1.75, for which the steady flow does not contain a separation bubble.

The asymptotic approximation of slightly supercritical oscillatory flows was verified by the numerical solution of the time-dependent Navier–Stokes equation using the finite volume method.

2. Formulation of the problem

The axisymmetric flow of an incompressible Newtonian fluid with kinematic viscosity ν^* in a cylinder of radius R^* and height H^*, with a lid rotating with angular velocity Ω^* at $z^* = H^*$ is considered. The flow is described by the momentum and continuity equations in a cylindrical system of coordinates (r, φ, z). Using the scales R^*, R^{*2}/ν^*, $\Omega^* R^*$ and $\rho^*(\Omega^* R^*)^2$ for length, time, velocity and pressure respectively, the dimensionless equations are

$$\left.\begin{aligned}
&\frac{\partial v_r}{\partial t}+v_r\frac{\partial v_r}{\partial r}+v_z\frac{\partial v_r}{\partial z}-\frac{v_\varphi^2}{r}=-\frac{\partial p}{\partial r}+\frac{1}{Re}\left(\frac{\partial^2 v_r}{\partial r^2}+\frac{1}{r}\frac{\partial v_r}{\partial r}+\frac{\partial^2 v_r}{\partial z^2}-\frac{v_r}{r^2}\right),\\
&\frac{\partial v_\varphi}{\partial t}+v_r\frac{\partial v_\varphi}{\partial r}+v_z\frac{\partial v_\varphi}{\partial z}+\frac{v_r v_\varphi}{r}=\frac{1}{Re}\left(\frac{\partial^2 v_\varphi}{\partial r^2}+\frac{1}{r}\frac{\partial v_\varphi}{\partial r}+\frac{\partial^2 v_\varphi}{\partial z^2}-\frac{v_\varphi}{r^2}\right),\\
&\frac{\partial v_z}{\partial t}+v_r\frac{\partial v_z}{\partial r}+v_z\frac{\partial v_z}{\partial z}=-\frac{\partial p}{\partial z}+\frac{1}{Re}\left(\frac{\partial^2 v_z}{\partial r^2}+\frac{1}{r}\frac{\partial v_z}{\partial r}+\frac{\partial^2 v_z}{\partial z^2}\right),
\end{aligned}\right\} \tag{1}$$

$$\frac{\partial v_r}{\partial r}+\frac{v_r}{r}+\frac{\partial v_z}{\partial z}=0. \tag{2}$$

The boundary conditions of an axisymmetric flow are imposed at the axis of the cylinder $(0 \leqslant z < \gamma, r = 0)$

$$v_r = v_\varphi = \frac{\partial v_z}{\partial r} = 0, \tag{3}$$

and the no-slip and no-penetration conditions are imposed on the rigid boundaries: on the cylindrical wall $(0 \leqslant z < \gamma, r = 1)$ and the stationary bottom of the cylinder $(0 \leqslant r \leqslant 1, z = 0)$

$$v_r = v_\varphi = v_z = 0, \tag{4}$$

and on the rotating lid of the cylinder ($0 \leqslant r < 1, z = \gamma$)

$$v_r = v_z = 0, \quad v_\varphi = r. \tag{5}$$

Here $Re = \Omega^* R^{*2}/\nu^*$ is the Reynolds number and $\gamma = H^*/R^*$ is the aspect ratio of the cylinder.

3. Numerical procedures

3.1. *Spectral Galerkin method*

The problem (1)–(5) was solved using the spectral Galerkin method with the basis functions defined by Gelfgat & Tanasawa (1993, 1994). The meridional velocity vector $\boldsymbol{v} = (v_r, v_z)^T$ and the azimuthal velocity component v_φ are approximated by the truncated series

$$\boldsymbol{v} \approx \sum_{i=0}^{N_r} \sum_{j=0}^{N_z} c_{ij}(t)\, \boldsymbol{u}_{ij}(r,z), \quad v_\varphi \approx \Omega(r,z) + \sum_{i=0}^{M_r} \sum_{j=0}^{M_z} d_{ij}(t)\, w_{ij}(r,z). \tag{6}$$

Here $c_{ij}(t)$ and $d_{ij}(t)$ are time-dependent coefficients to be found, N_r, N_z, M_r, M_z are numbers of basis functions used for the approximation of the unknown functions in the radial and axial directions; $\boldsymbol{u}_{ij}(r,z)$ and $w_{ij}(r,z)$ are vector and scalar basis functions defined as

$$\boldsymbol{u}_{ij}(r,z) = \left\{ \tfrac{1}{2} r \sum_{m=0}^{4} a_{im}\, T_{i+m}(r) \sum_{m=0}^{4} b_{jm}\, U_{j+m-1}(z/\gamma), \right.$$
$$\left. - \sum_{m=0}^{4} a_{im}\, \tilde{U}_{i+m-1}(r) \sum_{m=0}^{4} \frac{b_{jm}}{2(j+m)}\, T_{j+m}(z/\gamma) \right\}, \tag{7}$$

$$w_{ij}(r,z) = r(T_i(r) + p_i\, T_{i+1}(r))\,(T_j(z/\gamma) + q_{1j}\, T_{j+1}(z/\gamma) + q_{2j}\, T_{j+2}(z/\gamma)); \tag{8}$$

T_n and U_n are the Chebyshev polynomials of the first and second type respectively

$$T_n(x) = \cos[n \arccos(2x-1)], \quad U_n(x) = \frac{\sin[(n+1)\arccos(2x-1)]}{\sin[\arccos(2x-1)]}; \tag{9}$$

and

$$\tilde{U}_n(r) = T_{n+1}(r) + (n+1)\, r U_n(r). \tag{10}$$

Because of the relation between the Chebyshev polynomials $(\mathrm{d}/\mathrm{d}x)\, T_{n+1}(x) = 2(n+1)\, U_n(x)$ the basis functions (7) are divergence-free and the approximation of the velocity (6) is analytically divergence-free for any number of Galerkin modes.

The function $\Omega(r,z)$ is defined as the solution of the Stokes problem $\Delta v_\varphi = 0$ with the corresponding boundary conditions (3–5) for v_φ. Since the function $\Omega(r,z)$ satisfies the inhomogeneous boundary conditions (5), all the boundary conditions for the basis functions w_{ij} are homogeneous.

Substitution of (6)–(10) in the boundary conditions (3)–(5) defines a system of linear equations for the coefficients a_{im}, b_{jm}, p_i, q_{1j} and q_{2j}. Once these coefficients are determined (with the help of symbolic computations), the approximations (6) satisfy all boundary conditions and the continuity equation analytically.

The function $\Omega(r,z)$ is defined as the solution of the problem in the Stokes limit and is approximated by the truncated series

$$\Omega(r,z) = r \sum_{i=0}^{K_r} \sum_{j=0}^{K_z} \Omega_{ij}(T_i(r) + \tilde{p}_i\, T_{i+1}(r))\,(T_j(z/\gamma) + \tilde{q}_j\, T_{j+1}(z/\gamma)), \tag{11}$$

where the coefficients $\tilde{p}_i$ and $\tilde{q}_i$ are defined to satisfy the boundary conditions (4), (5) for v_φ. The $(K_r+1)K_z$ equations for the coefficients Ω_{ij} are obtained using the Galerkin method for the equation $\Delta\Omega = 0$. The other K_r equations for Ω_{ij} are defined by applying the collocation method at the K_r Chebyshev nodes along the boundary $z = \gamma$, $0 \leqslant r \leqslant 1$. Since the problem for $\Omega(r, z)$ is stationary and depends only on the aspect ratio of the cylinder, it was calculated once for each value of γ and was then treated as a known function.

The stream function ψ of the meridional flow is defined by

$$v_r = \frac{1}{r}\frac{\partial\psi}{\partial z}, \quad v_z = -\frac{1}{r}\frac{\partial\psi}{\partial r}.$$

Using (6), (7) an approximation of ψ may be written as

$$\psi = \sum_{i=0}^{N_r}\sum_{j=0}^{N_z} c_{ij}(t)\,\psi_{ij}(r, z), \tag{12}$$

where

$$\psi_{ij}(r, z) = \tfrac{1}{2}r^2 \sum_{m=0}^{4} a_{im}\,T_{i+m}(r) \sum_{m=0}^{4} \frac{b_{jm}}{2(j+m)}\,T_{j+m}(z/\gamma). \tag{13}$$

Once the Galerkin method with the basis functions (7), (8) is applied, the problem (1)–(5) is reduced to a system of ordinary differential equations (ODEs) for the time-dependent coefficients $c_{ij}(t)$ and $d_{ij}(t)$ that can be written in the following form (the summation convention on repeated indices is assumed):

$$\dot{X}_i = \frac{\mathrm{d}X_i(t)}{\mathrm{d}t} = F_i(X(t); Re) = L_{ij}\,X_j(t) + N_{ijk}\,X_j(t)\,X_k(t) + Q_i. \tag{14}$$

Here $i, j, k = \overline{1, (M_r+1)(M_z+1)+(N_r+1)(N_z+1)}$ and

$$\left.\begin{aligned} X_{i(M_z+1)+j+1} &= d_{ij}, & i &= \overline{0, M_r}, \quad j = \overline{0, M_z}, \\ X_{(M_r+1)(M_z+1)+i(N_z+1)+j+1} &= c_{ij}, & i &= \overline{0, N_r}, \quad j = \overline{0, N_z}. \end{aligned}\right\} \tag{15}$$

The matrices L_{ij}, N_{ijk}, Q_i contain coefficients of all the linear, bilinear and free terms of the equations, respectively.

3.2. *Linear stability analysis*

The completely explicit form of the system (14) allows us to use standard numerical methods developed for an ODE system both for obtaining stationary and non-stationary solutions and for the investigation of the stability of solutions. Thus, a stationary solution $\boldsymbol{X}^0$ of the system (14) is unstable if the Jacobian matrix calculated at $\boldsymbol{X} = \boldsymbol{X}^0$

$$J_{mk} = \left.\frac{\partial\dot{X}_m}{\partial X_k}\right|_{X=X^0} = L_{mk} + (N_{mkn} + N_{mnk})\,X^0_n \tag{16}$$

has at least one eigenvalue $\lambda = \lambda^r + \mathrm{i}\lambda^i$ with positive real part $\lambda^r > 0$. Thus, the investigation of stability for a given aspect ratio requires the determining of a value of *Re* such that the real part of the dominant eigenvalue (eigenvalue with the maximal real part) $\Lambda = \Lambda^r + \mathrm{i}\Lambda^i$ is zero: $\Lambda^r = 0$.

If for some value of *Re* the dominant eigenvalue has zero real part $\Lambda^r = 0$ and $\partial\Lambda^r/\partial Re \neq 0$, then $\Lambda^i \neq 0$ means a bifurcation to a periodic solution, called a Hopf

bifurcation, and $\Lambda^i = 0$ corresponds to a bifurcation from one stationary solution to another (Hopf 1942; Hassard, Kazarinoff & Wan 1981). In the case $\Lambda^i \neq 0$ the imaginary part Λ^i of the dominant eigenvalue gives an estimate of the circular frequency of the oscillatory solution branching from the steady state after the onset of the oscillatory instability.

The eigenvector V corresponding to the dominant eigenvalue Λ with $\Lambda^r = 0$ ($J_{mk} V_k = \Lambda V_m = \mathrm{i}\Lambda^i V_m$) defines the most unstable perturbation of the system (14). The most unstable perturbation of the flow may be calculated using the series (6) with coefficients c_{ij} and d_{ij} defined as components of the eigenvector V from (15). In the same way the limit cycle of the dynamical system (14), which develops as a result of the Hopf bifurcation, defines an approximation of the periodic solution of the problem (1)–(5).

3.3. *Approximation of slightly supercritical flows*

As was mentioned, the transition from the stationary solution $\boldsymbol{X}^0$ to a limit cycle takes place at a critical Reynolds number Re_{cr} when there exists an eigenvalue $\Lambda = \Lambda^r + \mathrm{i}\Lambda^i$ such that $\Lambda^r = 0$, $\partial\Lambda^r/\partial Re \neq 0$, $\Lambda^i = \omega_0 \neq 0$ and all other eigenvalues have negative real parts. Then there exists a small positive number $\epsilon > 0$, such that the asymptotic approximation of the limit cycle in the vicinity of Re_{cr} is defined by two parameters τ and μ as (Hassard *et al.* 1981)

$$Re = Re_{cr} + \mu\epsilon^2 + O(\epsilon^4), \tag{17a}$$

$$T(Re) = \frac{2\pi}{\omega_0}[1 + \tau\epsilon^2 + O(\epsilon^4)], \tag{17b}$$

$$\boldsymbol{X}(t; Re) = \boldsymbol{X}^0(Re_{cr}) + \epsilon\,\mathrm{Re}\left[V\exp\left(\frac{2\pi i}{T}t\right)\right] + O(\epsilon^2). \tag{17c}$$

Here $(Re - Re_{cr})$ is the supercriticality, T is the period of oscillations, and $\boldsymbol{X}$ is the asymptotic solution of the ODE system (14) for the Reynolds number defined in (17*a*). It should be noticed that the parameter μ defines the direction of bifurcation: the bifurcation is supercritical if $\mu > 0$, and subcritical if $\mu < 0$.

The algorithm for the numerical calculation of the coefficients τ and μ is described by Hassard *et al.* (1981). These coefficients are defined as

$$\mu = -\frac{\mathrm{Re}(\xi)}{\alpha^r}, \quad \tau = -\frac{1}{\omega_0}(\mathrm{Im}(\xi) + \mu\alpha^i), \tag{18}$$

where

$$\alpha^r = \left.\frac{\mathrm{d}\Lambda^r}{\mathrm{d}\,Re}\right|_{Re=Re_{cr}}, \quad \alpha^i = \left.\frac{\mathrm{d}\Lambda^i}{\mathrm{d}\,Re}\right|_{Re=Re_{cr}}, \quad \xi = \frac{G_{21}}{2} + \frac{i}{2\omega_0}(g_{20}g_{21} - 2|g_{11}|^2 - \tfrac{1}{3}|g_{02}|^2), \tag{19}$$

$$g_{20} = 2\boldsymbol{U}^T f_{20}, \quad g_{02} = 2\boldsymbol{U}^T \bar{f}_{20}, \quad g_{11} = 2\boldsymbol{U}^T f_{11}, \tag{20}$$

$$f_{20} = \frac{\partial^2}{\partial\zeta^2}\boldsymbol{F}[\boldsymbol{X}^0 + \mathrm{Re}(V\zeta); Re_{cr}]|_{\zeta=0}, \quad f_{11} = \frac{\partial^2}{\partial\zeta\,\partial\bar{\zeta}}\boldsymbol{F}[\boldsymbol{X}^0 + \mathrm{Re}(V\zeta); Re_{cr}]|_{\zeta=0}, \tag{21}$$

$$G_{21} = \frac{\partial^3}{\partial^2\zeta^2\,\partial\bar{\zeta}}\{2\boldsymbol{U}^T\boldsymbol{F}[\boldsymbol{X}^0 + \mathrm{Re}(V\zeta + w_{20}\zeta^2 + w_{11}\zeta\bar{\zeta}); Re_{cr}]\}|_{\zeta=0}. \tag{22}$$

In (19)–(22) $\boldsymbol{F}(\boldsymbol{X}; Re)$ is the right-hand side of the ODE system (14), $\zeta = x + \mathrm{i}y$ is a complex number, an overbar denotes complex conjugate, and $\boldsymbol{U}$ and V are respectively

the left and right eigenvectors of the Jacobian matrix $\boldsymbol{J}$ defined in (16). The vectors $\boldsymbol{w}_{11}$ and $\boldsymbol{w}_{20}$ are solutions of the following systems of linear algebraic equations

$$\boldsymbol{J}\boldsymbol{w}_{11} = -\boldsymbol{h}_{11}, \quad [\boldsymbol{J} - 2\mathrm{i}\omega_0 \boldsymbol{I}]\,\boldsymbol{w}_{20} = -\boldsymbol{h}_{20}, \tag{23}$$

where $\boldsymbol{h}_{ij} = [\boldsymbol{I} - 2\,\mathrm{Re}(\boldsymbol{V}\boldsymbol{U}^T)]\boldsymbol{f}_{ij}$ and $\boldsymbol{I}$ is the identity matrix.

The stability of the branching limit cycle is determined by the largest non-zero Floquet exponent β which may be approximated as (Hassard *et al.* 1981)

$$\phi = \beta\epsilon^2 + O(\epsilon^4), \quad \beta = -2\alpha^r\mu. \tag{24}$$

The limit cycle is stable if $\phi < 0$ and unstable if $\phi > 0$. In the problem considered the Hopf bifurcation takes place when the Reynolds number exceeds a critical value. This means that α^r is always positive (Λ^r grows with growing Re). Then, as follows from (24), the supercritical Hopf bifurcations lead to stable limit cycles ($\mu > 0 \Rightarrow \phi < 0$), while limit cycles corresponding to the subcritical bifurcations are unstable ($\mu < 0 \Rightarrow \phi > 0$).

For the dynamical system (14) the expressions (21) and (22) may be evaluated analytically, giving

$$\left.\begin{aligned} f_{20,k} &= \tfrac{1}{2}[N_{kij}(V_i^r V_j^r - V_i^i V_j^i) + \mathrm{i}N_{kij}(V_i^r V_j^i - V_i^i V_j^r)], \\ f_{11,k} &= \tfrac{1}{2}N_{kij}(V_i^r V_j^r + V_i^i V_j^i), \\ G_{21} &= \tfrac{1}{2}U_i(N_{ijm} + N_{imj})[2w_{11,j} V_m + w_{20,j}\bar{V}_m]. \end{aligned}\right\} \tag{25}$$

The numerical process was organized in the following way: first, for an initial value of the Reynolds number Re^0 a stationary solution of the ODE system (14) was calculated with the Newton method; second, eigenvalues of the Jacobian matrix (16) were calculated with the QR decomposition algorithm. These two steps were repeated for the next value of the Reynolds number, usually chosen as $1.01Re^0$. Then the real part Λ^r of the dominant eigenvalue was considered as a function of the Reynolds number, and the value of the critical Reynolds number Re_{cr} corresponding to $\Lambda^r(Re_{cr}) = 0$ was found with the secant method. When the value of Re_{cr} is found, the linear stability analysis is completed. The last step is the application of the algorithm (18)–(25) which requires the calculation of the derivative $\mathrm{d}\Lambda/\mathrm{d}Re$ at $Re = Re_{cr}$ and the right and left eigenvectors of the Jacobi matrix. At this step the values of the dominant eigenvalue and the eigenvectors were calculated with the inverse iteration algorithm.

3.4. *Verification of the method*

Test calculations were carried out to check the convergence of stationary solutions, of the critical values, and of the characteristics of slightly supercritical flows. Stationary solutions, critical values and asymptotically approximated slightly supercritical flows calculated by the Galerkin method were compared with results obtained by independent calculations in other studies (see figure 12*b*) and by the direct numerical solution of the time-dependent Navier–Stokes equation (see §4.4 and the Appendix).

To validate the asymptotic approximation of the slightly supercritical flows, the asymptotic expansions (17) were substituted in the non-stationary equations and residuals, averaged over the period of oscillations, were calculated. The test calculations were carried out for $\gamma = 1.5$, 2.5 and 3.25. Details of the test calculations are presented in the Appendix.

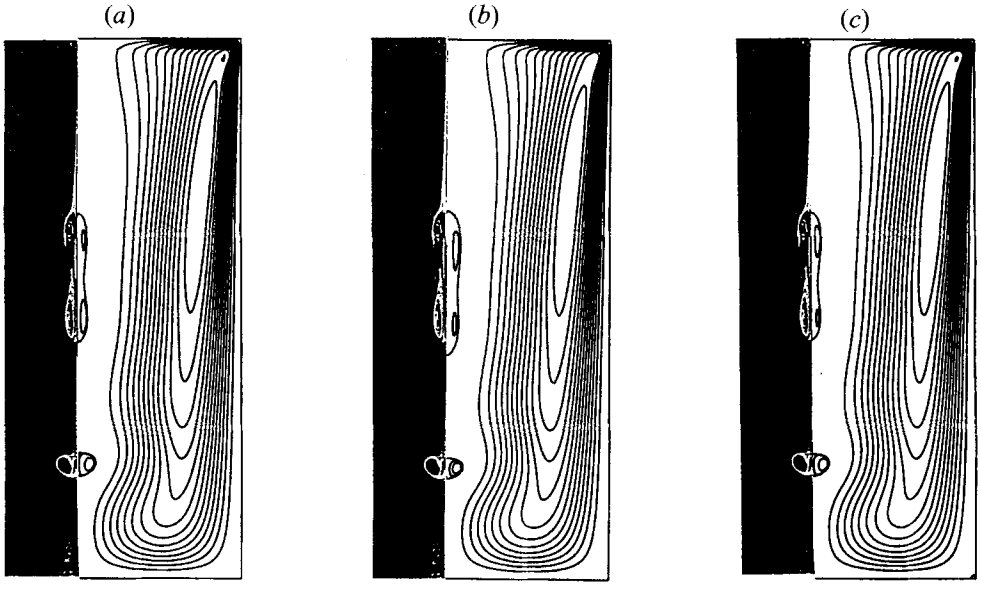

FIGURE 1. Meridional flow streamlines, $\gamma = 3.25$, $Re = 2752$. Comparison of numerical results with the experimental photograph of Escudier (1984). (*a*) Calculation with the Galerkin method using 34×34 basis functions. (*b*) Calculation with the finite volume method using the 100×100 stretched grid. (*c*) Calculation with the finite volume method using the 200×200 stretched grid.

A comparison for the case $\gamma = 3.25$, $Re = 2752$ is shown in figure 1. In this case three vortex bubbles were observed in the experiment of Escudier (1984). As seen from figure 1 the experimental result is well reproduced with 34×34 functions (figure 1*a*), as well as with a 200×200 stretched finite volume grid (figure 1*c*). At the same time the upper recirculation region is resolved inaccurately with a 100×100 grid (figure 1*b*).

To verify the asymptotic approximation of the limit cycle expressions (17) were substituted in the non-stationary ODE system (14) and a residual *Res* averaged over a period of oscillations was estimated as

$$Res = \frac{1}{N}\frac{1}{T}\int_0^T \|\dot{X}(t) - F(X(t); Re)\| \, \mathrm{d}t, \tag{26}$$

where T is the period of oscillations, N is the total number of degrees of freedom in (14), and $\|\cdot\|$ stands for Euclidean norm. Note that in view of the asymptotic expansion (17) and the algorithm (18)–(25) the leading term of *Res* should be of order ϵ^2. The dependence of *Res* on ϵ^2 is shown in figure 2 for the case $\gamma = 1.5$. It indicates that *Res* remains proportional to ϵ^2 for $\epsilon^2 \leqslant 10^{-3}$. This gives an upper estimate $(Re - Re_{cr}) \leqslant 10^{-3}\,\mu$ for the interval of the Reynolds numbers where the expansion (17*c*) may be used. Note that this estimate shows for which Reynolds numbers the expansion (17) gives a correct asymptotic approximation of the limit cycle of the dynamic system (14). On the other hand, this estimate does not guarantee the stability of the limit cycle, and its convergence to the limit cycle of the hydrodynamic problem considered. The latter may be checked by comparison of the asymptotic approximations with the results of direct numerical simulation (§4.4).

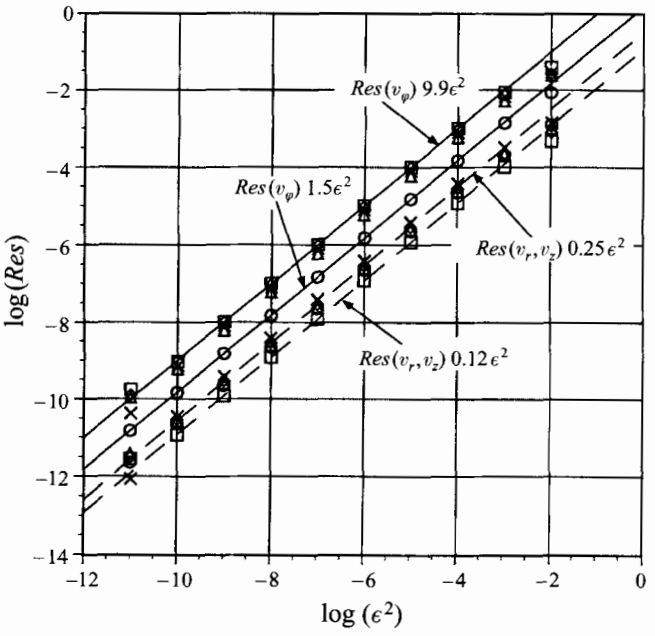

FIGURE 2. The averaged residual of (*a*) meridional flow $Res(v_r, v_z)$ and (*b*) azimuthal velocity $Res(v_\varphi)$ versus ϵ^2: △, calculation with 16×16 functions; ○, calculation with 20×20 functions; □, calculation with 24×24 functions.

4. Main results

An example of the vortex breakdown in a cylinder with aspect ratio $\gamma = 1.5$ is illustrated in figure 3. In this case the separation bubble appears at $Re \approx 1075$, grows, then diminishes with growing Re, and disappears at $Re \approx 1920$.

This appearance of a separation vortex bubble is not yet completely understood. Brown & Lopez (1990) argued that the 'generation' of negative azimuthal vorticity η ($\eta = \partial v_r/\partial z - \partial v_z/\partial r$) is responsible for the appearance of a separation bubble. On this basis, the criterion for the vortex breakdown may be related to the change of sign of η near the axis of the cylinder, or to the change of the sign of $\Phi = (\partial/\partial z)(\Gamma^2/r^3)$, where $\Gamma = rv_\varphi$, which may be interpreted as a source term in the equation for η

$$\frac{D\eta}{Dt} = \Phi + \frac{1}{Re}\left(\Delta\eta - \frac{\eta}{r^2}\right) \tag{27}$$

(see also Davidson 1989; Lopez 1994). Change of sign of η and Φ for the case $\gamma = 1.7$ is illustrated in figure 4. It is seen that Φ becomes negative for $Re < 300$ (figure 4*b*, *c*), and η changes its sign near the axis for $Re < 750$ (figure 4*d*, *e*). On the other hand, the patterns of the streamlines at $Re = 750$, and especially at $Re = 300$, do not indicate significant changes in the meridional flow.

To obtain more information about the behaviour of η and Φ with increasing Re we carried out additional calculations for the cases $\gamma = 1$ and 0.5, when no separation vortex bubble appears. The corresponding results are plotted in figures 5 and 6. It is seen that in these cases η and Φ also change their signs near the axis (Φ changes its sign at lower Re than η does), but separation vortex bubbles never appear. This means that the change of sign of η or Φ does not necessarily indicate the appearance of a recirculation zone in the flow. Thus, the appearance of a recirculation zone in the flow

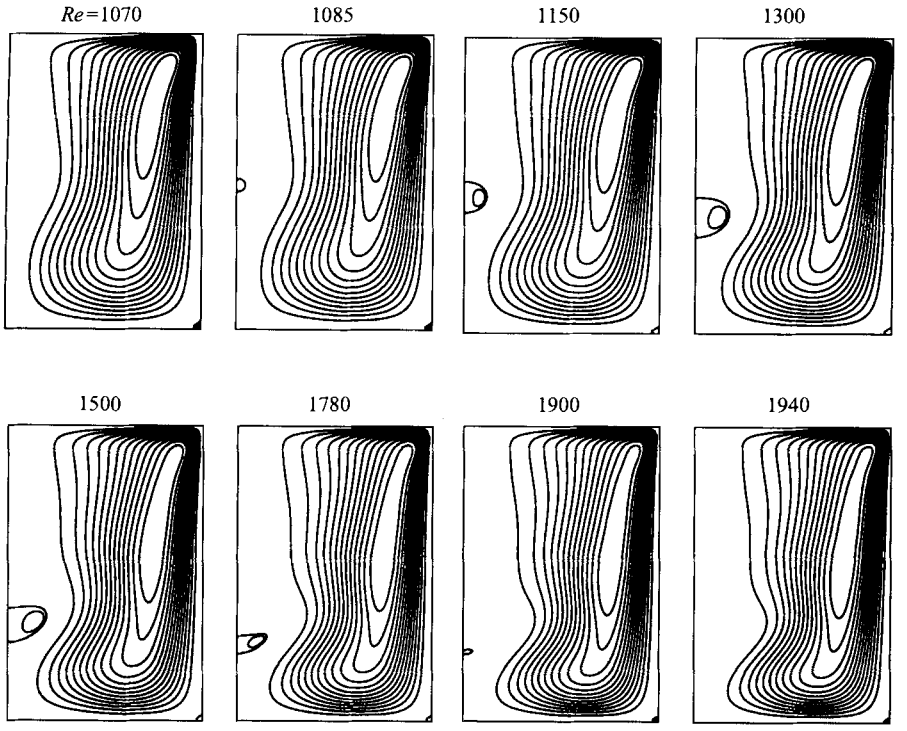

FIGURE 3. Appearance and disappearance of the vortex breakdown, $\gamma = 1.5$. 20×20 functions.

cannot be completely explained by change of sign of η and Φ. In fact, since the term $r\eta$ mathematically plays the role of a source term in the kinematic relationship between η and ψ,

$$\frac{\partial^2 \psi}{\partial z^2} + r\frac{\partial}{\partial r}\left(\frac{1}{r}\frac{\partial \psi}{\partial r}\right) + r\eta = 0, \tag{28}$$

the existence of a local maximum and a local maximum of ψ (main meridional vortex and separation vortex bubble) necessarily means that the sign of η changes. Thus, if at a certain value of Re, Re_b say, a separation vortex bubble (local minimum of ψ) appears in the flow, this means that η is already negative in the vicinity of the bubble and changed its sign at a lower $Re = Re_\eta$, such that $Re_\eta < Re_b$. The same may be said about the change of sign of Φ, which is the source term in (27) and changes its sign at $Re = Re_\Phi$ such that $Re_\Phi < Re_\eta$. This means that the change of signs of η and Φ may be considered as a necessary condition for the appearance of the separation vortex bubble (specifically, B-type vortex breakdown, Escudier 1988; Delery 1994).

The following is an attempt at an heuristic explanation of change of signs of η and Φ and appearance of the separation vortex bubble. These features of the flow may be understood from the analysis of the isolates of v_φ, ψ, η and Φ plotted in figures 4, 5 and 6.

By definition

$$\Phi = \frac{\partial}{\partial z}\left(\frac{\Gamma^2}{r^3}\right) = \frac{v_\varphi}{r}\frac{\partial v_\varphi}{\partial z}$$

changes its sign when the sign of the derivative $\partial v_\varphi/\partial z$ changes ($v_\varphi > 0$). Analysis of figure 4(*a–c*) shows that $\partial v_\varphi/\partial z$ becomes negative when the meridional flow is intensive

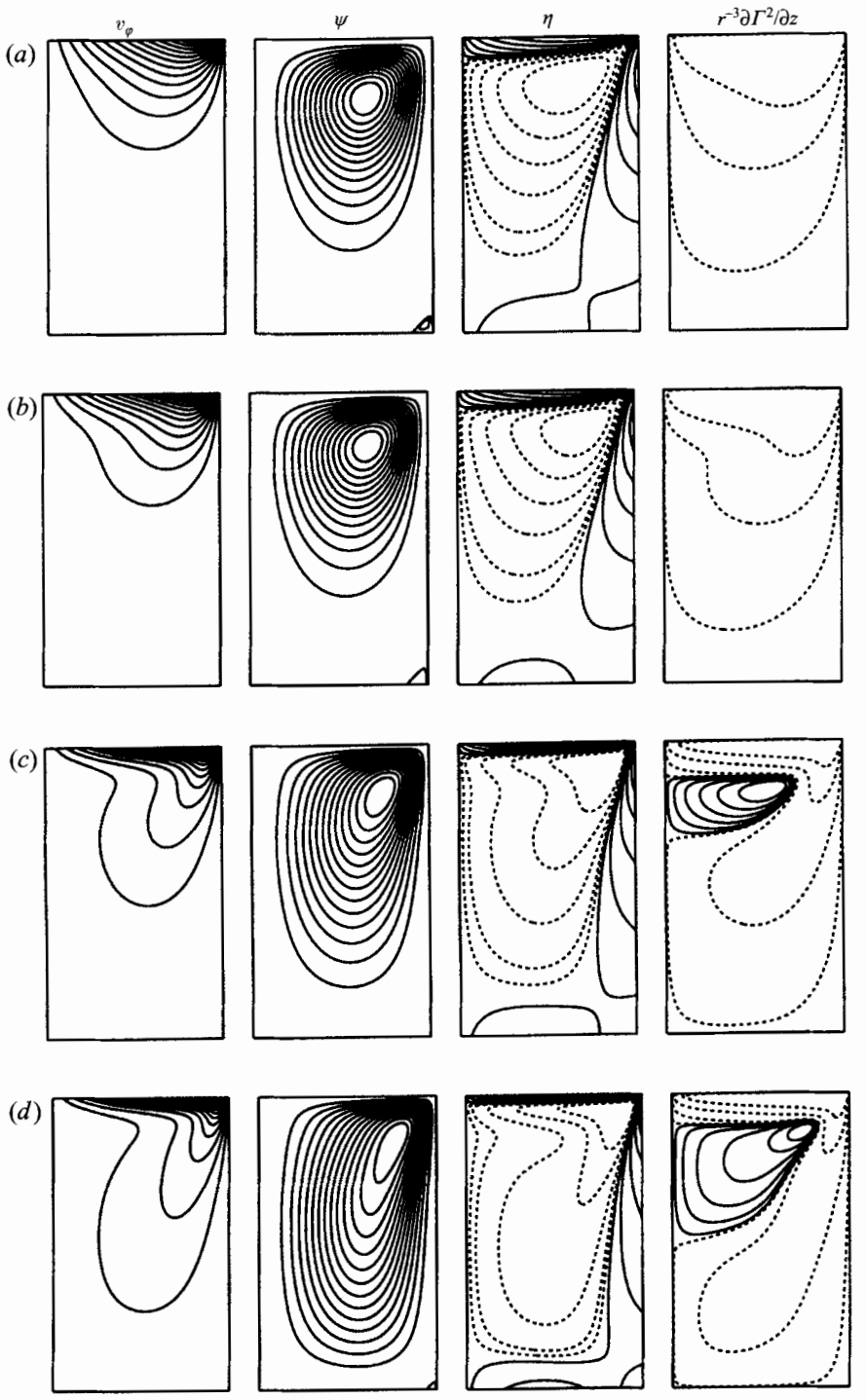

FIGURE 4(*a–d*). For caption see page 13.

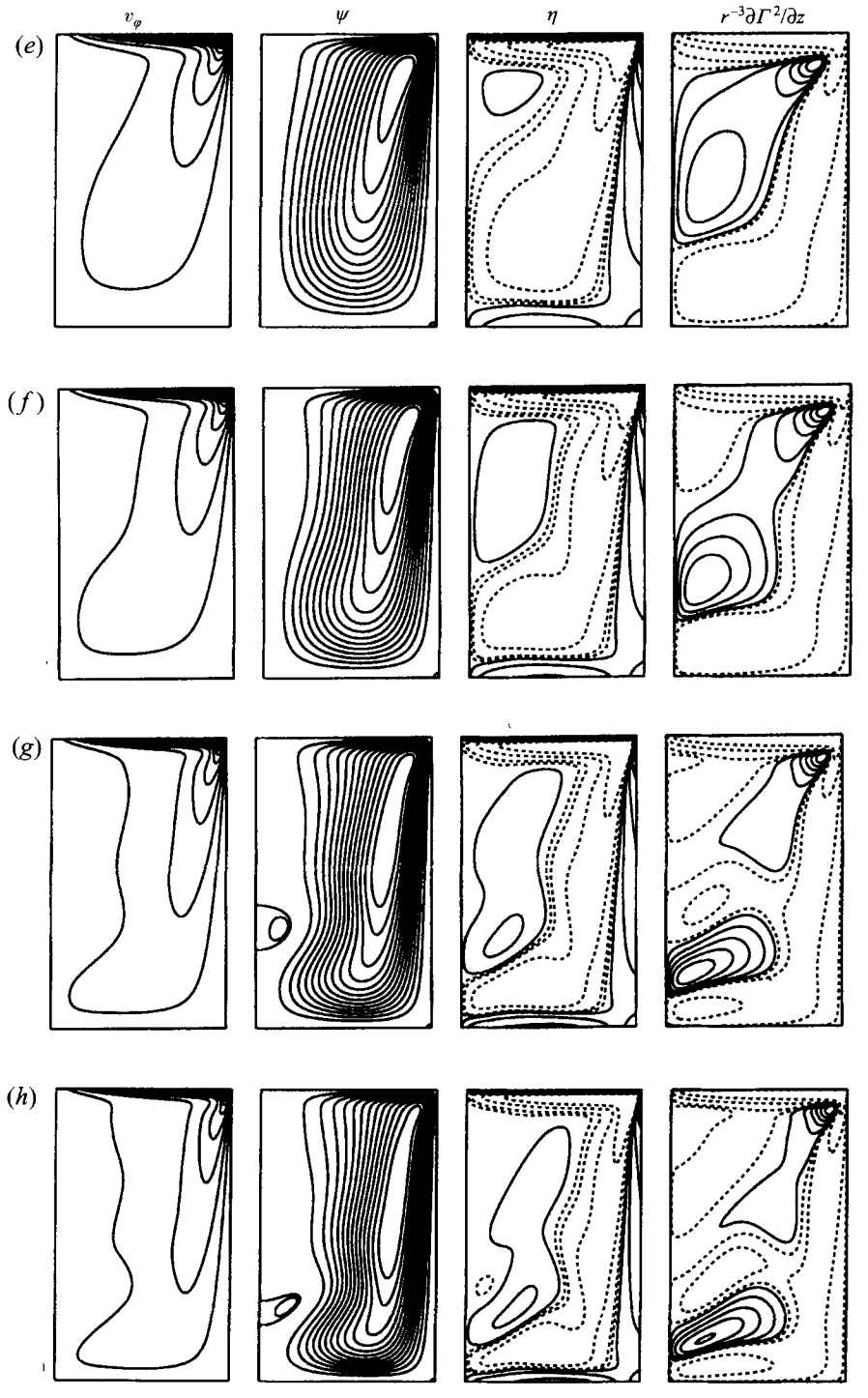

FIGURE 4(*e–h*). For caption see facing page.

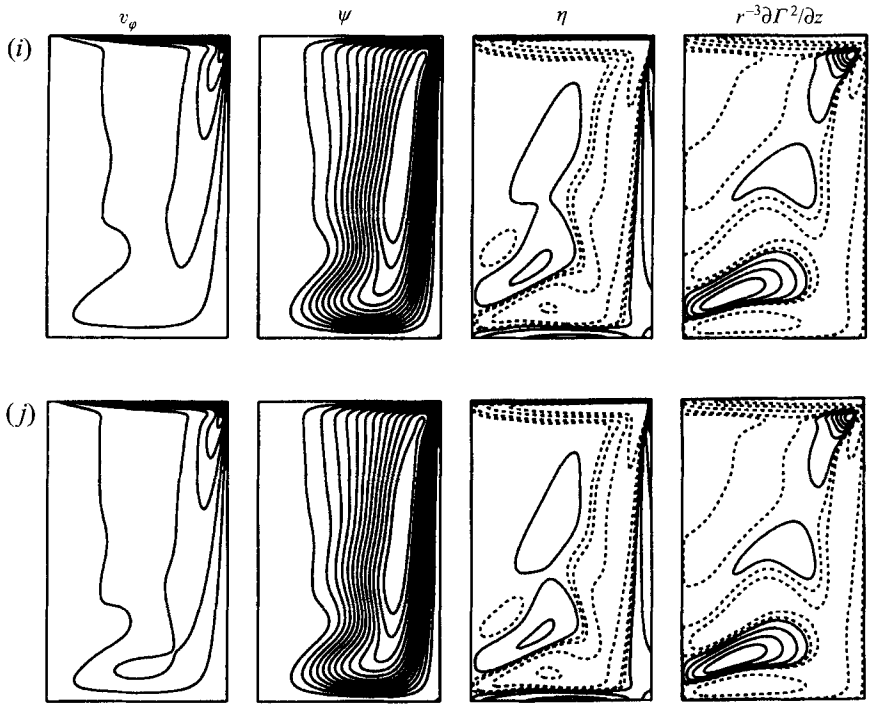

FIGURE 4. Isolines of v_φ, ψ, η and Φ for $\gamma = 1.7$ and Reynolds number equal to (*a*) 50, (*b*) 100, (*c*) 300, (*d*) 500, (*e*) 750, (*f*) 1000, (*g*) 1500, (*h*) 2000, (*i*) 2400, (*j*) 2700. Negative isolines are dotted.

enough to make the convection of the azimuthal velocity v_φ comparable with its diffusion. The meridional flow transports large azimuthal velocity from the edge of the lid downwards along the wall and then along the bottom towards the axis. Since the rotational momentum rv_φ has to be preserved, v_φ grows with the decrease of r. In other words one can say that when $v_r < 0$ (motion towards the axis) the Coriolis acceleration $(-v_r v_\varphi/r)$ acts in the direction of rotation so as to increase v_φ. As a result, the distribution of $v_\varphi(z, r^*)$ along a cylindrical surface $r = r^*$ has a local maximum at a certain value $z = z_1$, and a local minimum at $z = z_2$, such that $z_2 > z_1$ (figure 4*c–f*, 5*c–h*, 6*d–i*). This means that $(\partial v_\varphi/\partial z)(r^*, z_1 < z < z_2) < 0$ and consequently $\Phi(r^*, z_1 < z < z_2) < 0$.

On the cylindrical surface $r = r^*$ the centrifugal acceleration v_φ^2/r also has a local maximum at $z = z_1$. This means that at this point the fluid is forced towards the cylindrical wall more vigorously than above and below. This leads to a deformation of stream surfaces such that they become concave (as seen from inside the curve, figures 4*f*, 5*f–h*, 6*h*, *i*). The concave shape of the streamsurfaces for $Re > 1000$ is a common feature of the flows illustrated in figures 4–6. Hence, along with the necessary conditions for the vortex breakdown – change of signs of η and Φ (Brown & Lopez 1990; Lopez 1994) – and with the obvious sufficient criterion – existence of a recirculation zone – there is another possible condition: concave shape of the streamsurfaces near the axis of swirling flow.

Consider now the azimuthal vorticity $\eta = \partial v_r/\partial z - \partial v_z/\partial r$ in that region of the rising part of the flow ($v_z = (1/r)\partial\psi/\partial r > 0$) where η changes sign (see figures 4*e*, 5*f*, 6*h*). The derivative $\partial v_z/\partial r$ is negative in this region, because v_z reaches its maximal value near the axis and decreases with growth of r. This means that in this region of the flow (in which

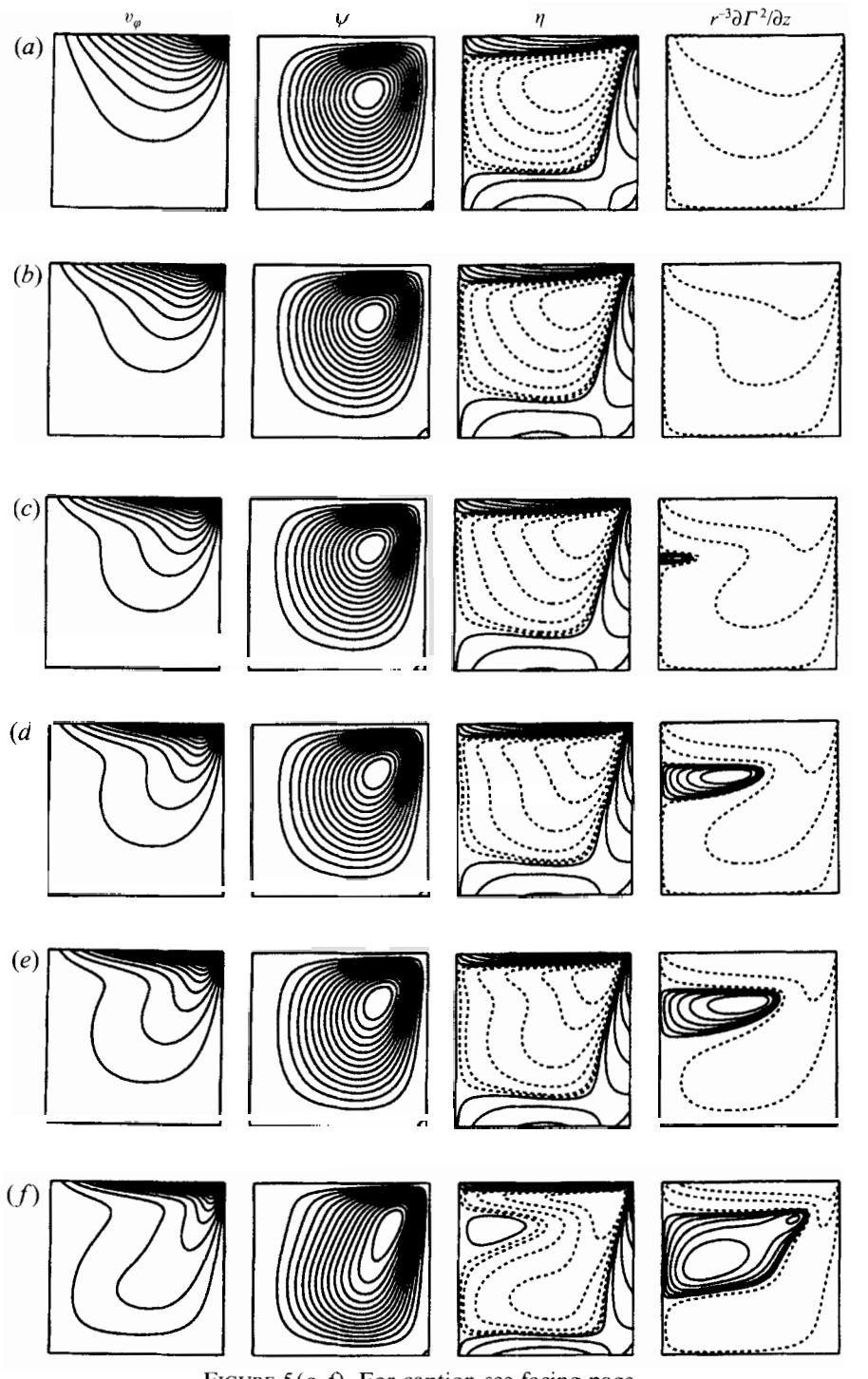

FIGURE 5(*a–f*). For caption see facing page.

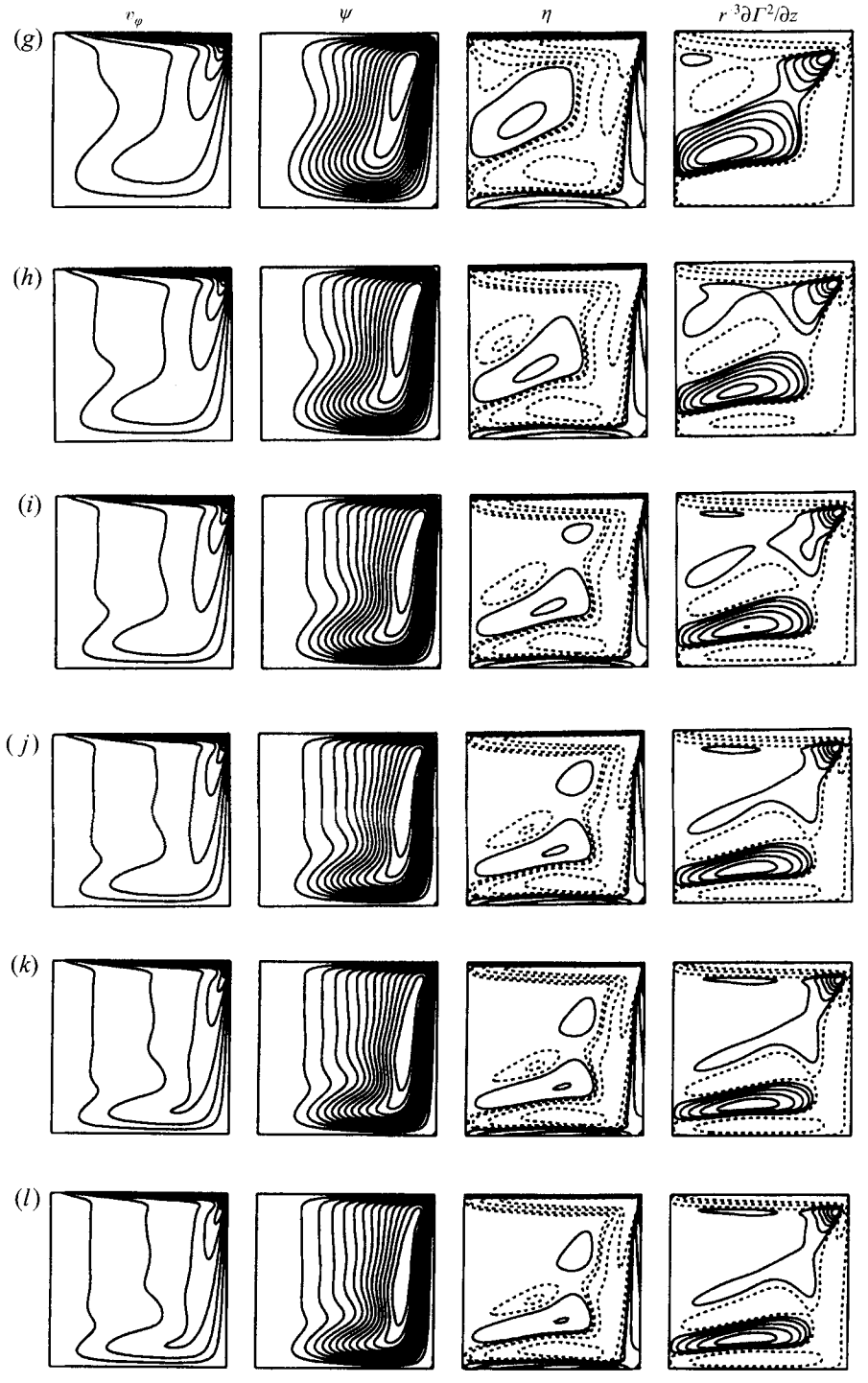

FIGURE 5. Isolines of v_φ, ψ, η and Φ for $\gamma = 1$ and Reynolds number equal to (*a*) 50, (*b*) 100, (*c*) 150, (*d*) 200, (*e*) 250, (*f*) 500, (*g*) 1000, (*h*) 1500, (*i*) 2000, (*j*) 2500, (*k*) 3000, (*l*) 3151 (= Re_{cr}).

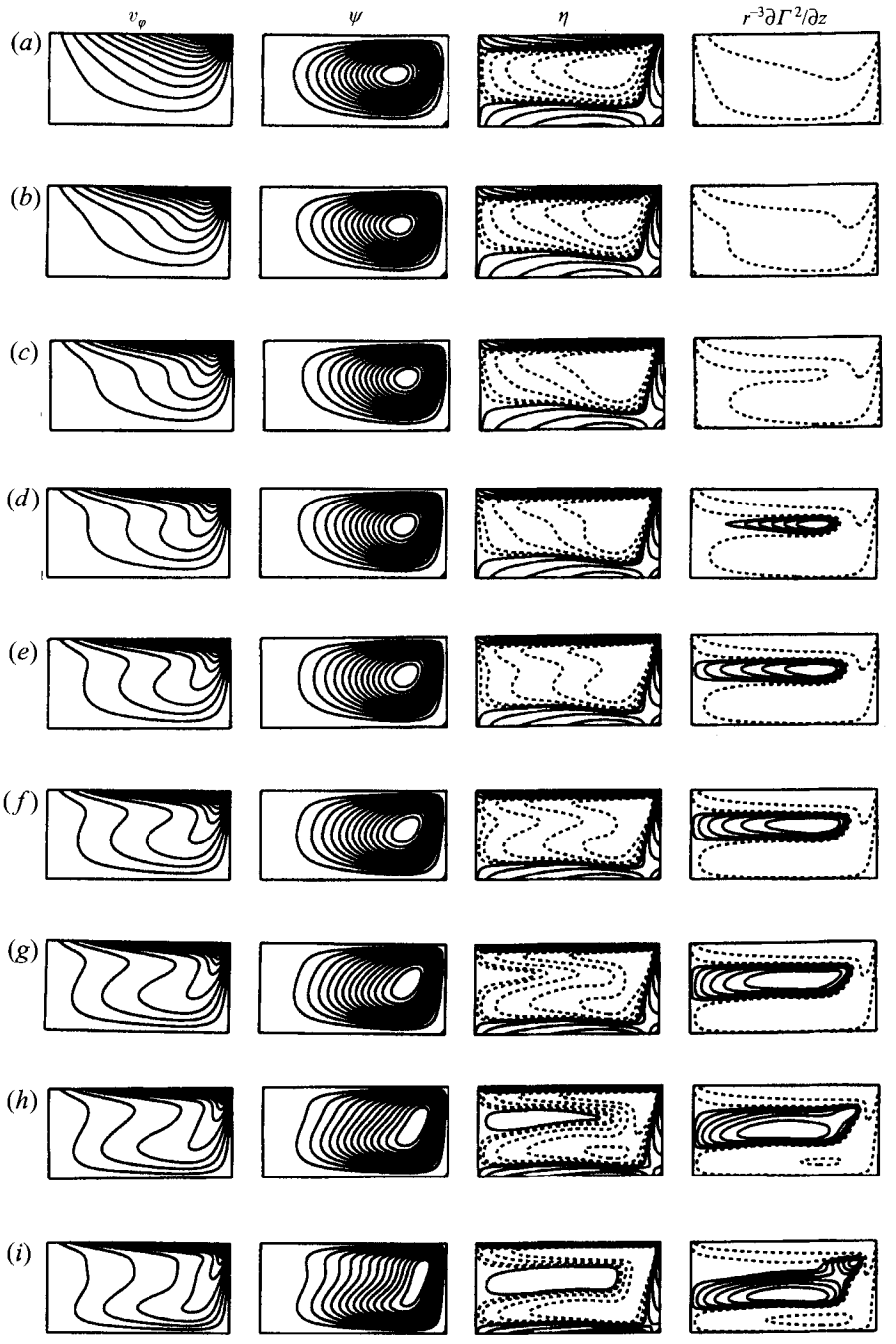

FIGURE 6. Isolines of v_φ, ψ, η and Φ for $\gamma = 0.5$ and Reynolds number equal to (*a*) 100, (*b*) 200, (*c*) 300, (*d*) 400, (*e*) 500 (*f*) 600, (*g*) 750, (*h*) 1000, (*i*) 1500.

there is no recirculation) the term $-\partial v_z/\partial r$ in the definition of η cannot contribute to the change of the sign of vorticity from positive to negative. The other term, $\partial v_r/\partial z = -(1/r)\partial^2\psi/\partial z^2$, in the definition of η can be negative only if $\partial^2\psi/\partial z^2 > 0$. This can happen only on the part of the surface $r = r^*$ where the function $\psi(r^*, z)$ is concave. Thus, a concave form of the streamsurfaces is another necessary condition for the

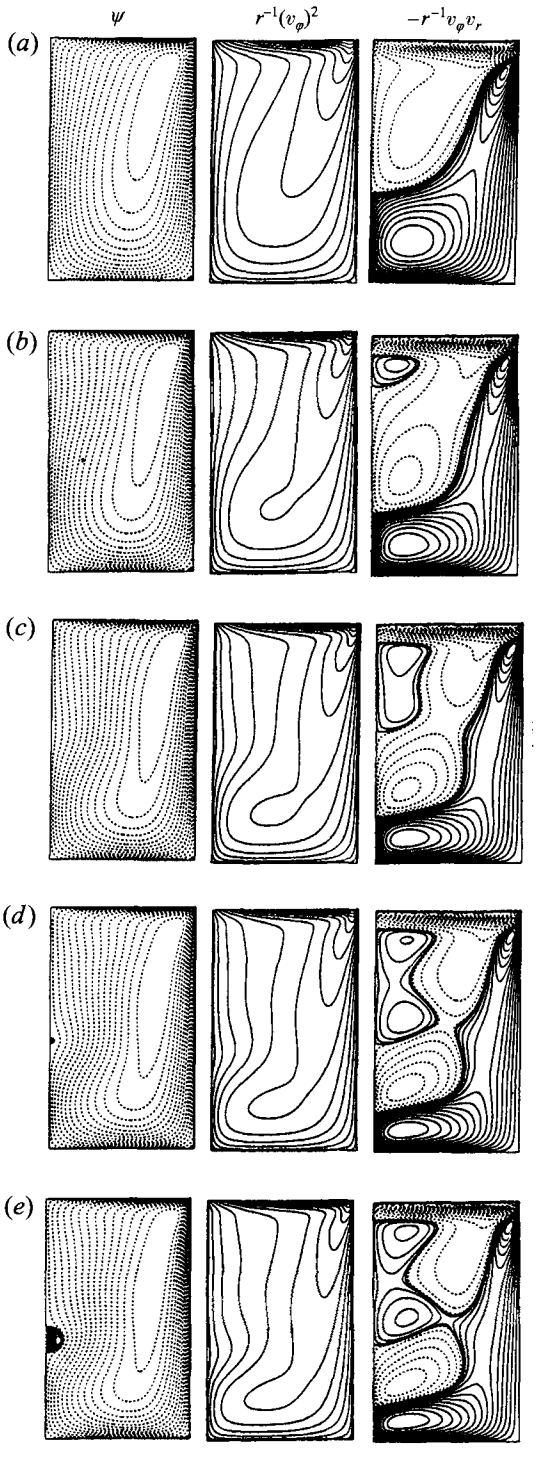

FIGURE 7. Isolines of the stream function ψ, the centrifugal acceleration v_φ^2/r, and the Coriolis acceleration $-v_r v_\varphi/r$ for the case $\gamma = 1.7$ and Reynolds number equal to (*a*) 700, (*b*) 900, (*c*) 1100, (*d*) 1220, (*e*) 1300.

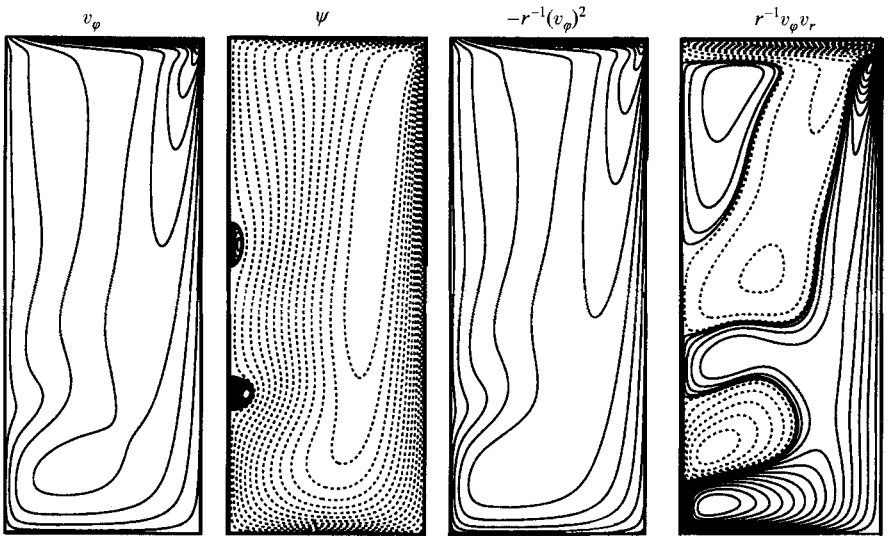

FIGURE 8. Isolines of the azimuthal velocity v_φ, stream function ψ, centrifugal acceleration v_φ^2/r and the Coriolis acceleration $-v_r v_\varphi/r$ for the case $\gamma = 2$, $Re = 2000$.

appearance of negative azimuthal vorticity near the axis of the cylinder. As was previously shown, the concave form of the streamsurfaces is the consequence of the local growth of the centrifugal acceleration which, in its turn, is the consequence of the convective transport of v_φ.

Thus, we have shown that the convective transport of v_φ results in the non-monotone axial distribution of the centrifugal acceleration, which is the main reason for the change of signs of η and Φ. Furthermore, we can assume that the appearance of a recirculation zone (separation vortex bubble) may be due to the same cause. In fact, the swirling flow considered is created by the centrifugal and the Coriolis forces. The Coriolis force acts in the azimuthal direction and cannot create any meridional recirculation. The centrifugal force acts in the radial direction from the axis towards the cylindrical boundary and creates the main meridional recirculation. One may assume that if the described local maximum of the centrifugal acceleration (centrifugal force) is large enough, this can produce additional weak radial motion directed from the axis towards the boundary, which may lead to a meridional recirculation.

This assumption is illustrated in figures 7 and 8. On the concave part of a streamline the radial velocity changes its sign from positive to negative (figure 7*b*). This results in the change of sign of the Coriolis acceleration $-v_r v_\varphi/r$ (v_φ is always non-negative). The negative Coriolis acceleration increases the azimuthal velocity such that one can see weak local maxima and minima in the axial distribution of the centrifugal acceleration v_φ^2/r (figure 7*d*, *e*). This local decrease and increase of the centrifugal acceleration may lead to the appearance of additional radial motion which may result in a recirculation. This assumption gains support in figure 8 which shows the case with two separation vortex bubbles ($\gamma = 2.5$, $Re = 2000$). In this case the axial distribution of the Coriolis acceleration near the axis has three regions of positive and three regions of negative values. This results in additional waviness in the axial distribution of the centrifugal acceleration which has more local extrema than in the case $\gamma = 1.7$.

It should be mentioned that the function Φ defined above may be interpreted as the derivative of the centrifugal acceleration with respect to z. One can see from figure 4(*g*,

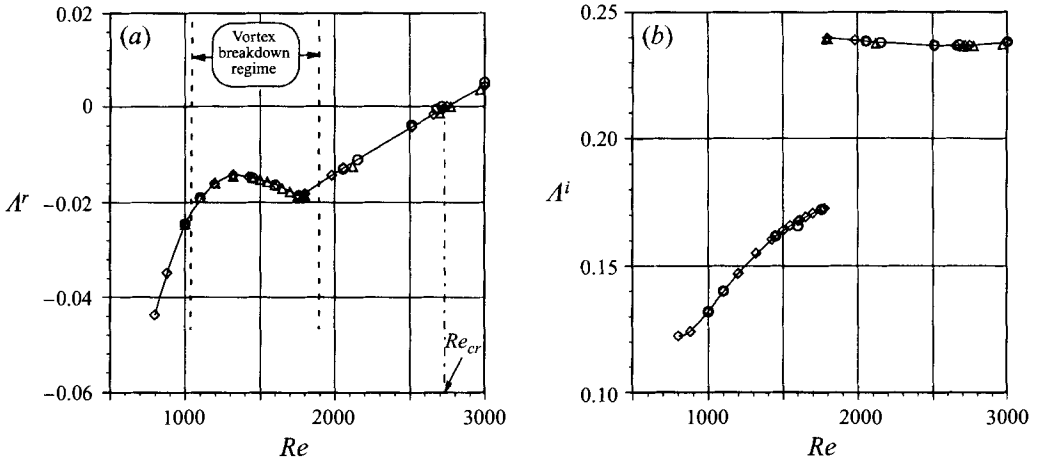

FIGURE 9. Dependence of the real and imaginary parts of the dominant eigenvalue on the Reynolds number, $\gamma = 1.5$: △, calculation with 16×16 functions; ◇, 18×18 functions; ○, 20×20 functions.

h) that the separation vortex bubble appears in the region where Φ changes its sign from negative to positive, in other words when the centrifugal force begins to increase with the growth of z.

4.1. *Stability of the vortex breakdown*

There have been many claims (see Lugt & Abboud 1987; Tsitverblit 1993) that vortex breakdown in the disk–cylinder system is not the result of an instability, but a continuous variation of the steady flow that takes place with continuously increasing Reynolds number. A direct analysis of the stability of the flow with respect to all infinitely small axisymmetric perturbations is presented here for the first time. Another question which has not been answered yet is whether the appearance and disappearance of the second and the third separation bubbles is a continuous evolution or an instability of the single-separation-bubble flow.

Figures 9–11 show the dependence of the real and imaginary parts of the dominant eigenvalue of the Jacobian matrix (16) on the Reynolds number for aspect ratios 1.5, 2, and 2.5. The vertical dashed lines show the boundaries of the appearance and disappearance of the separation bubbles. The changes in the slope of $\Lambda^r(Re)$ and the discontinuity of $\Lambda^i(Re)$ correspond to the switch of the dominant perturbation mode. To verify the conclusions, results for different numbers of Galerkin functions are presented in the figures.

Figure 9 corresponds to the case $\gamma = 1.5$, illustrated in figure 3. With increasing Reynolds number the flow before, during, and after the vortex breakdown is stable, as indicated by $\Lambda^r < 0$. A switch of the dominant perturbation mode takes place at $Re \approx 1800$, which has no connection with the appearance and disappearance of the vortex breakdown at $Re \approx 1075$ and $Re \approx 1920$, respectively. The oscillatory instability sets in at $Re_{cr} = 2724$ after the vortex breakdown disappears.

In the case $\gamma = 2.0$ (figure 10) there are four successive dominant modes of the perturbations when the Reynolds number increases from 1000 to 3300. The vortex breakdown appears at $Re \approx 1452$ and disappears at $Re \approx 3019$, while between $Re \approx 1830$ and $Re \approx 2283$ two separation bubbles exist. The oscillatory instability sets in at $Re_{cf} = 2580$ when the vortex breakdown still exists but after disappearance of the second separation bubble. The boundaries of existence of the second separation bubble

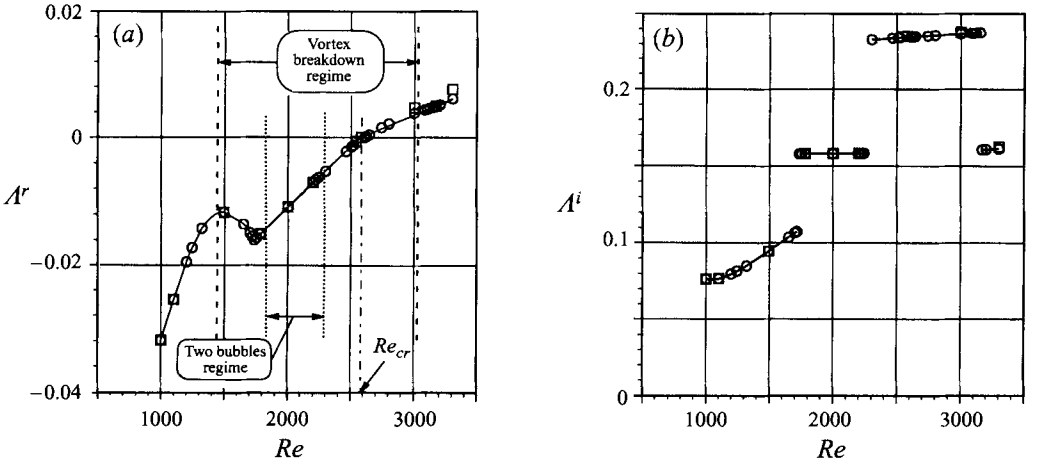

FIGURE 10. Dependence of the real and imaginary parts of the dominant eigenvalue on the Reynolds number, $\gamma = 2.0$: ○, calculation with 20×20 functions; □, 24×24 functions.

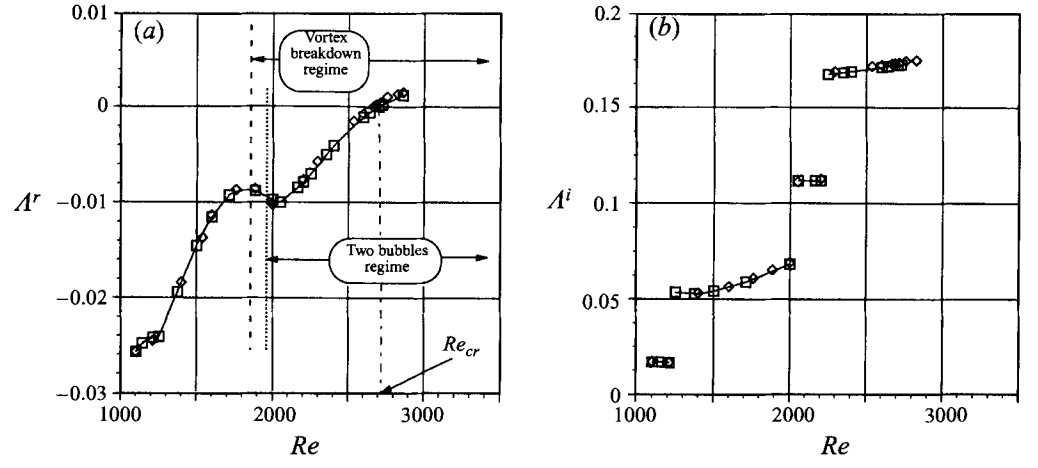

FIGURE 11. Dependence of the real and imaginary parts of the dominant eigenvalue on the Reynolds number, $\gamma = 2.5$: □, calculation with 24×24 functions; ◇, 16×30 functions.

are close to the boundaries of the second dominant mode (see figure 10) but do not coincide with them. In general, no connection is observed between the changes of the dominant perturbation mode or instability of the flow and the appearance and disappearance of the first or the second separation bubble.

In the case $\gamma = 2.5$ (figure 11) there are also four successive dominant modes of the perturbations when the Reynolds number changes from 1100 to 2850. The vortex breakdown appears at $Re \approx 1840$ and the second separation bubble appears at $Re \approx 1950$. The oscillatory instability sets in at $Re_{cr} = 2706$ when both separation bubbles still exist. The vortex breakdown disappears in this case far above Re_{cr}. As in the previous case, no connection is observed between a switch of the dominant perturbation mode or instability of the flow and the appearance of the first or the second separation bubble.

The results presented in figures 9–11 show that the flow considered here is linearly

stable with respect to all infinitely small axisymmetric perturbations before and after the vortex breakdown appears. This means that the vortex breakdown observed in the system is a result of the continuous evolution of the stable stationary flow with increasing Reynolds number. Furthermore, the change from a one-separation-bubble to a two-separation-bubble flow structure, as well as the reverse change from two- to one-separation-bubble flow, are also not connected with any stability phenomena; neither is the disappearance of the vortex breakdown.

4.2. *Oscillatory instability onset*

The critical parameters Re_{cr}, ω_{cr}, corresponding to the onset of the oscillatory instability (which according to our analysis is a result of a Hopf bifurcation), were calculated for aspect ratio varying from 1 to 3.5 (figure 12). The results are compared with the experimental data of Escudier (1984) (figure 12*a*) and the numerical results of Daube & Sørensen (1989), Lopez & Perry (1992), Christensen *et al.* (1993), Tsitverblit (1993), and present numerical solution with the finite volume method (figure 12*b*). Note that the previously published results for $Re_{cr}(\gamma)$ are limited to the range $2 \leqslant \gamma \leqslant 2.75$, and results for $\omega_{cr}(\gamma)$ are available only for $\gamma = 2$ and 2.5. Results of our stability analysis for $Re_{cr}(\gamma)$ and $\omega_{cr}(\gamma)$ cover the whole range from $\gamma = 1$ (below the appearance of a steady vortex breakdown bubble) to $\gamma = 3.5$ (where only Escudier's experiments are available). Several points of $\omega_{cr}(\gamma)$ for $\gamma < 2.5$ were calculated with the finite volume method (§4.4). Calculated points of $Re_{cr}(\gamma)$ and $\omega_{cr}(\gamma)$ are shown in figure 12(*c*).

One can see from figure 12(*b*) that for aspect ratio $\gamma < 3$ the results obtained here are in good agreement with all the previous calculations as well as with the present time-marching calculations (§4.4) except for one single result of Daube & Sørensen (1989) for $\gamma = 2.5$.

For $\gamma > 3$ no numerical data are available for comparison. Comparison with the experimental results of Escudier (1984) shows that the critical Reynolds numbers obtained numerically are larger than those obtained in the experiment. On the other hand, a switch of the dominant perturbation mode is observed between $\gamma = 2.9$ and 3 (figure 12) both in the experiment and in our stability analysis. The reasons of the discrepancy between experimental and numerical results will be discussed in §4.3.

For $1 < \gamma < 1.8$ again no numerical or experimental data are available for comparison. Since the calculations for this case are easier than for larger aspect ratios, and convergence in the case $\gamma = 1.5$ has been checked (see table 2), these results may also be considered as sufficiently accurate.

The curves $Re_{cr}(\gamma)$ and $\omega_{cr}(\gamma)$ indicate that there are three different modes of the most unstable perturbation. The eigenvector V of the Jacobian matrix (16) corresponding to the dominant eigenvalue $\Lambda(J_{mk} V_k = \Lambda V_m, \Lambda^r = 0)$ defines the most unstable perturbation of the stationary solution of the dynamical system (14). The oscillatory instability sets in when the Reynolds number exceeds the value Re_{cr} as the appearance of oscillations with exponentially growing amplitude. The distribution of this amplitude in the flow region coincides, within multiplication by a constant, with the distribution of the modulus of the most unstable perturbation (recall that the perturbation is a complex function, see (17)). This means that the patterns of the absolute value of the perturbation describe the amplitude of the oscillatory state near the threshold of instability, and may be used for the analysis of the physical causes of the instability.

Perturbations of the meridional stream function ψ and the φ-component of the momentum $\mathscr{M}_\varphi = rv_\varphi$ were chosen for plotting since they were found to give the best

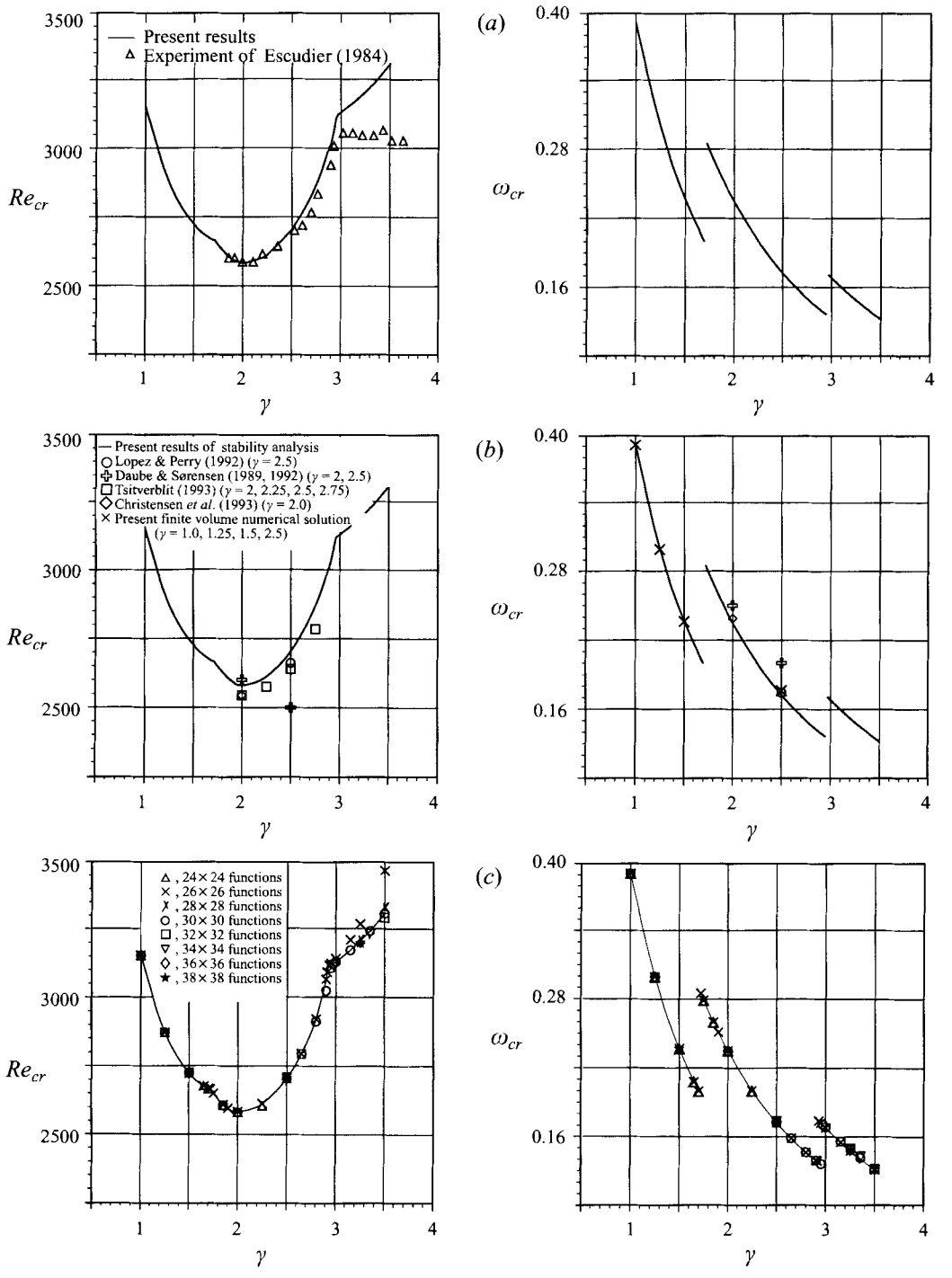

FIGURE 12. Stability diagram corresponding to the onset of the oscillatory instability. Critical Reynolds number (left) and critical cycle frequency (right) versus aspect ratio (*a*) Comparison of the present results with the experiment of Escudier (1984); (*b*) comparison of the present results with the independent calculations; (*c*) present results obtained with a different discretization.

representation of the changes in the perturbation with varying Re and γ. Isolines of the absolute values of the perturbation are plotted in figure 13. The absolute value of perturbations (amplitude of the most unstable mode) is chosen for plotting because this property does not depend on time and phase. It may be easily used for comparison of results obtained with different spatial discretizations as well as with different numerical approaches. At the same time the isolines plotted in figure 13 describe the distribution of the amplitude of the oscillations of ψ and $\mathscr{M}_\varphi$ (see (17)).

Note that there is an abrupt change in the spatial structure of the perturbation between $\gamma = 1.72$ and 1.73, and between $\gamma = 2.91$ and 2.93 corresponding to the discontinuities in the slopes of the neutral curve in figure 12.

The most noticeable change is observed in the perturbation of the stream function. In the case of smaller aspect ratio (figure 13*a*) it occurs as the sudden appearance of an additional saddle point near the vertical rigid wall of the cylinder, and the appearance of a weak local maximum of the perturbation near the stationary bottom. In the case of larger aspect ratio (figure 13*b*) the change is even more noticeable and manifests itself as the appearance of the additional maximum in the central part of the cylinder together with an additional saddle point near the vertical wall.

Changes in the perturbation of $\mathscr{M}_\varphi$ are noticeable only in the part of the cylinder located between the axis and the rigid cylindrical wall. Perturbation in this region is relatively weak in comparison with the perturbation located near the cylindrical wall and the bottom (figure 13). The maximum values, as well as the maximum gradient of the perturbation of $\mathscr{M}_\varphi$, are located near the vertical wall and the stationary bottom of the cylinder. This feature of the perturbation of $\mathscr{M}_\varphi$ does not change with the change of the aspect ratio and does not depend on the existence of the separation vortex bubble. The existence of this almost unchanging feature of the perturbation allows us to suppose that the reason for the oscillatory instability is the same for all the values of aspect ratio considered, and is connected with the disturbances of rotation near the vertical wall, the top, and the bottom of the cylinder. It should be mentioned that this possible reason for the onset of oscillatory instability is not connected with the existence of a separation vortex bubble in the flow. Moreover, perturbations of the rotational and meridional components of the flow, as well as gradients of the perturbations, are weak near the axis where the vortex breakdown (whichever way it is defined) takes place. This allows the conclusion that the oscillatory instability is not caused by the vortex breakdown.

4.3. *Weakly nonlinear analysis of Hopf bifurcation*

The application of the asymptotic expansion (17) requires the calculation of two parameters μ and τ (figure 14). Since the values of μ and τ depend on the scaling of the eigenvectors V and U (as may be seen from (17)–(23)), these parameters cannot be directly compared for different values of γ and different spatial discretizations. It was found that scaling of the coefficients μ and τ by the coefficient β from the expansion of the Floquet exponent (24) allows us to obtain smooth functions for $\mu(\gamma)$ and $\tau(\gamma)$ and to compare results calculated with different numbers of basis functions.

The sign of μ shows the direction of the Hopf bifurcation corresponding to the neutral curve (figure 12*a*). The bifurcation is found to be *supercritical* for all values of the aspect ratio (figure 14*a*). The supercritical character of the Hopf bifurcation considered was postulated previously on the basis of a straightforward simulation of the flow by Daube & Sørensen (1989) for $\gamma = 2$ and by Tsitverblit (1993) for $\gamma = 2.5$. The present results prove the supercritical character of the axisymmetric Hopf bifurcation for the whole interval $1 \leqslant \gamma \leqslant 3.5$.

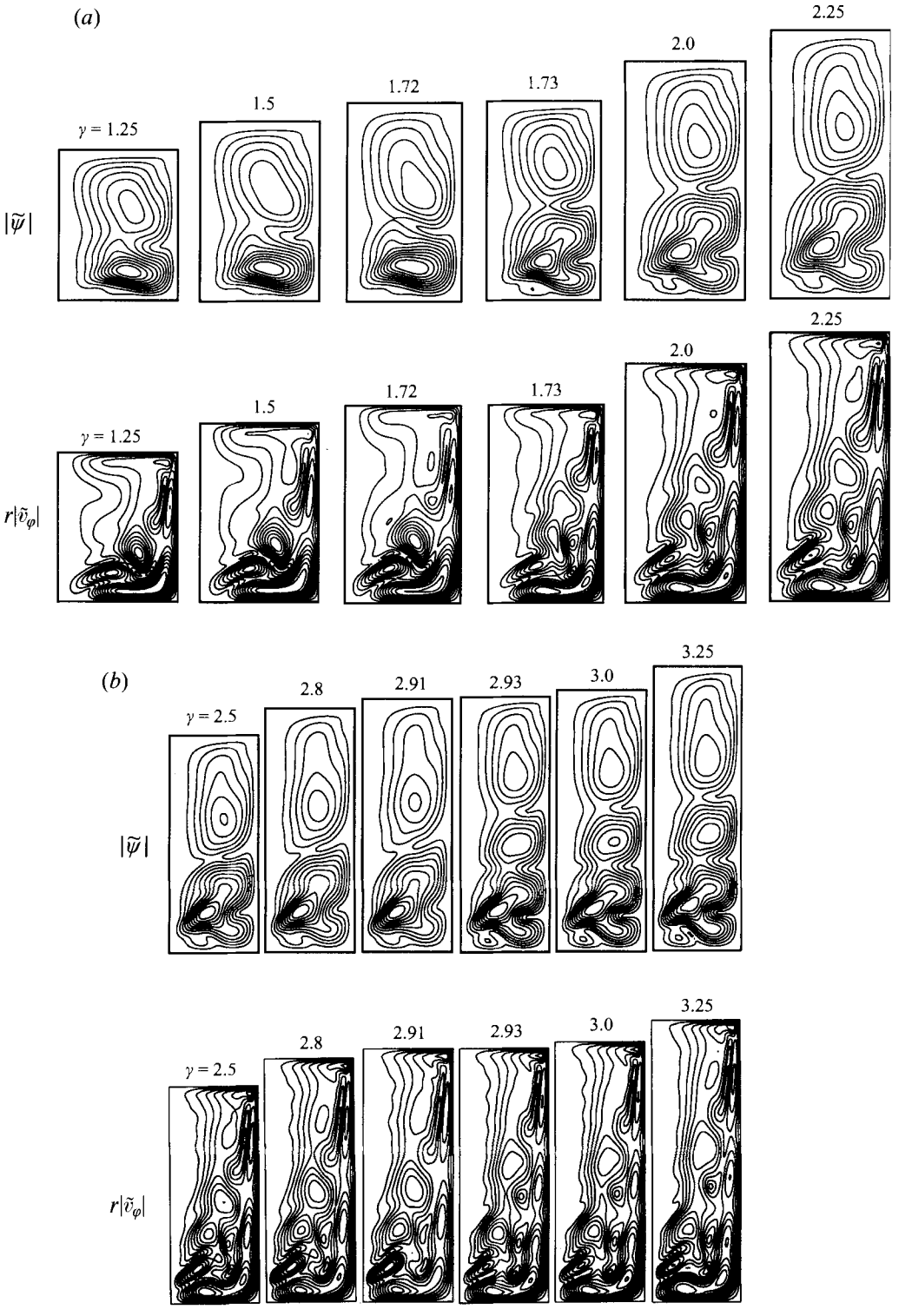

FIGURE 13. Isolines of the absolute value of the most unstable perturbation (tilde denotes perturbation). Upper part: perturbation of the meridional stream function. Lower part: perturbation of the moment of the angular velocity. Abrupt change of the most unstable perturbation mode takes place between (*a*) $\gamma = 1.72$ and $\gamma = 1.73$; and (*b*) $\gamma = 2.91$ and $\gamma = 2.93$.

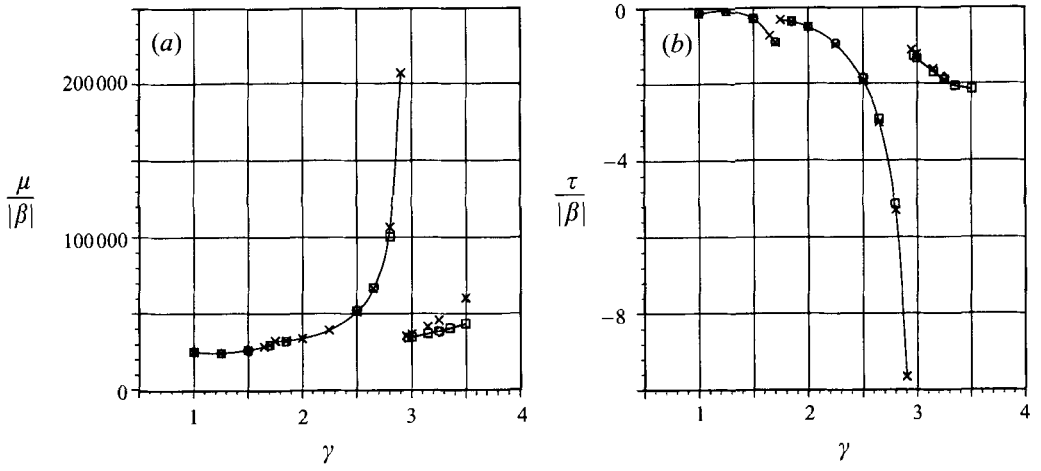

FIGURE 14. Coefficients of the asymptotic expansion of the limit cycle (17): ○, calculation with 24×24 functions; ×, 26×26 functions; □, 30×30 functions; ◇, 38×38 functions.

Since the axisymmetric Hopf bifurcation is supercritical for all values of the aspect ratio, steady flows below the neutral curve plotted in figure 12 are stable with respect to all infinitely small axisymmetric perturbations. This means that the discrepancy between the predicted and the experimental critical values of the Reynolds number for large aspect ratios ($\gamma > 3$, figure 12*a*) is due to three-dimensional effects and cannot be explained by a subcritical axisymmetric bifurcation.

According to Escudier's experiments the results of the oscillatory instability for $\gamma > 3$ is a precession of the separation bubble around the axis, i.e. a transition from an *axisymmetric* to an *asymmetric* flow. The present numerical analysis does not include asymmetric perturbations and cannot describe such a transition. On the other hand, results of linear and weakly nonlinear axisymmetric stability analyses completely exclude the possibility of explaining the experimental observations in terms of an axisymmetric instability. However, both experimental and numerical neutral curves have breaks at approximately the same value of the aspect ratio, $\gamma \approx 3$. This means that there are two possible routes for the transition from an axisymmetric to an asymmetric state. The first is a switch of the most unstable mode corresponding to an instability of the steady state: an asymmetric perturbation mode becomes more unstable than an axisymmetric mode when the aspect ratio exceeds the value of approximately 3. This switch of modes may be found by an analysis of the stability of the initial axisymmetric steady flow with respect to asymmetric perturbations and means that the closeness of the breaks in the slopes of the experimental and numerical axisymmetric neutral curves is fortuitous.

Another possibility is the following: the axisymmetric oscillatory flow resulting from a supercritical axisymmetric Hopf bifurcation is unstable with respect to asymmetric perturbations (note that according to the slightly supercritical analysis the axisymmetric limit cycle is stable with respect to axisymmetric perturbations). If the latter instability is subcritical, the final asymmetric oscillatory flow may be observed below the neutral curve corresponding to the linear axisymmetric instability. In this case an investigation of the stability of axisymmetric oscillatory flow is necessary for a correct description of the transition.

The value of τ which describes the deviation of the period of oscillations from the result of the linear stability analysis is plotted in figure 14(*b*). As one can see, τ is

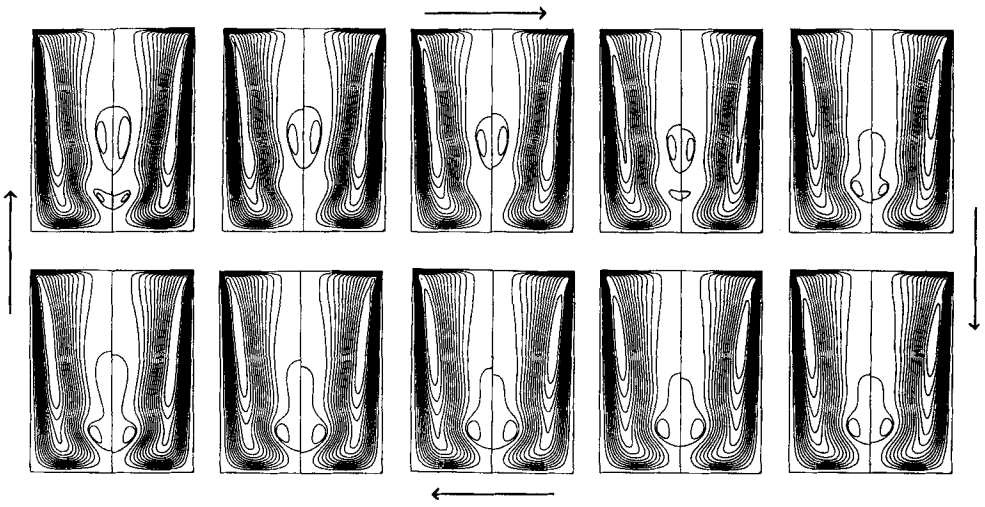

FIGURE 15. Instantaneous streamlines of the meridional flow plotted for equal time intervals $0.1T$ covering the complete period. $\gamma = 2.5$, $Re = 2765$, $Re - Re_{cr} \approx 59$, $\epsilon^2 \approx 5 \times 10^{-5}$. Calculation with 38×38 basis functions (left) and with 150×150 stretched grid (right).

negative for all values of the aspect ratio, which means that the real period of oscillations is slightly less than that obtained by the linear stability analysis. The deviation of the period from the result of linear analysis may be estimated as $(\tau/\mu)\ (Re - Re_{cr})$. The ratio τ/μ does not exceed 10^{-4} and the critical period $2\pi/\omega_{cr}$ is always more than 10 (figure 12). According to the test calculations, the asymptotic expansion (17) is valid for $(Re - Re_{cr})$ of order 100 or less, so that the deviation of the period from its critical value is relatively small.

The instantaneous streamlines of a slightly supercritical flow for $\gamma = 2.5$, $Re = 2765$ are shown in figure 15. The parameters correspond to the result of the direct numerical solution of the non-steady problem presented in figure 6(*a*) of Lopez (1990). It is noteworthy that the results of linear stability analysis in this case are close to those obtained by Lopez (1990) and Lopez & Perry (1992) (see figure 12*b*). Moreover, the snapshots of the asymptotically approximated stream function are very close to those obtained by numerical solution of the full unsteady Navier–Stokes equations (figure 15). This result reproduces the coupling and decoupling of two separation bubbles during one period of oscillations as reported by Lopez (1990).

Other interesting features of supercritical flows were observed for smaller values of the aspect ratio, $\gamma \leqslant 1.75$, when the oscillatory instability takes place after the separation vortex bubble disappears (Escudier 1984). Thus, for $\gamma = 1.5$ the critical Reynolds number is approximately $Re_{cr} \approx 2724$ and the steady flow at $Re = Re_{cr}$ does not contain a separation bubble. With a small increase of the Reynolds number above Re_{cr} weak pulsations of the main meridional vortex are observed. With further increase of the Reynolds number a weak pulsating separation bubble appears at $Re \approx 2760$. The size of the separation bubble and the fraction of the period during which it exists increase with growing Reynolds number. This is illustrated in figure 16 for $Re = 2800$ when the pulsating separation bubble exists during approximately 3/10 of the period. Note that in the case of $\gamma = 1.5$ the steady separation vortex bubble disappears at $Re \approx 1900$ (figure 3), and the appearance of a pulsating separation bubble at much larger Reynolds number $Re \approx 2760$ is quite unexpected. The result is obtained as an

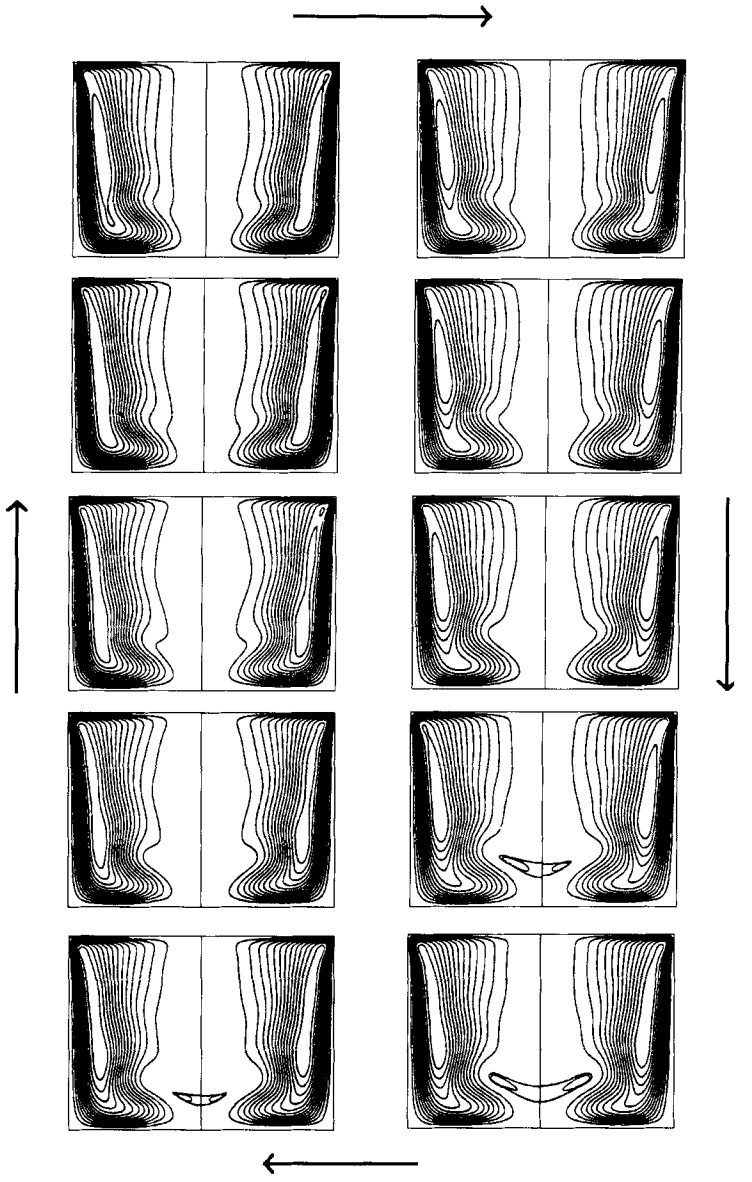

FIGURE 16. As figure 15 but for $\gamma = 1.5$, $Re = 2800$, $Re - Re_{cr} \approx 76$, $\epsilon^2 \approx 2 \times 10^{-4}$.

asymptotic approximation and is verified by the numerical solution of the unsteady Navier–Stokes equation (figure 16).

Furthermore, in the case of $\gamma = 1.25$ the slightly supercritical flow at $Re = 3050$ contains two distinct pulsating separation bubbles (figure 17). The critical Reynolds number in this case is approximately $Re_{cr} \approx 2871$, so that the supercriticality in this case is equal to 179. With the growth of the Reynolds number the size of both oscillating bubbles increases (figure 18, $Re = 3100$). During a period of oscillation both separation vortex bubbles increase and decrease in axial and radial directions but do not coincide with each other (figures 17 and 18).

For even smaller aspect ratio, $\gamma = 1$, only one oscillating separation bubble appears at approximately $Re \approx 3500$. The critical Reynolds number for $\gamma = 1$ is $Re_{cr} \approx 3151$,

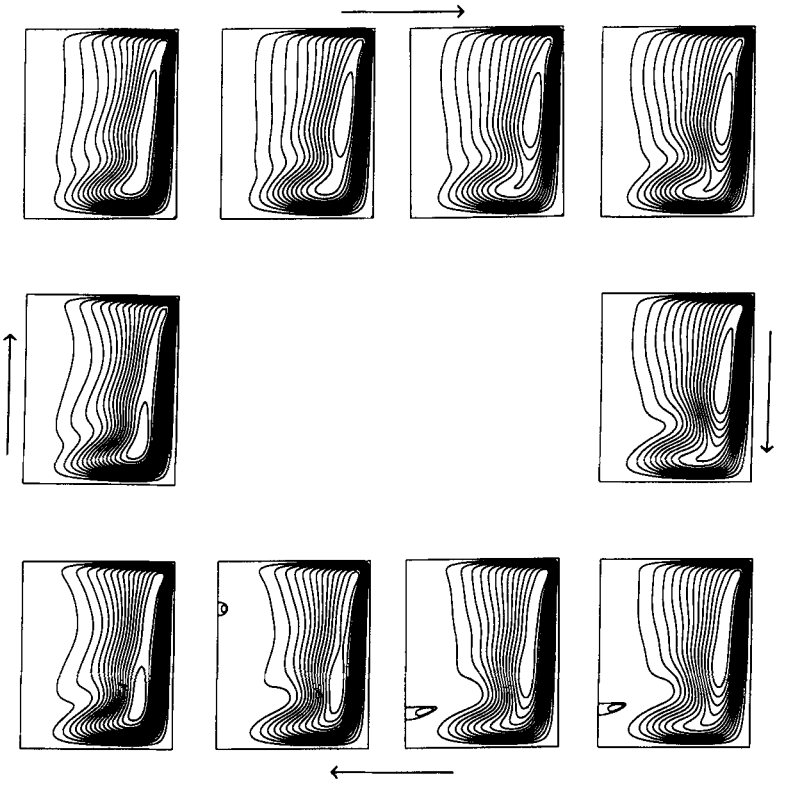

FIGURE 17. As figure 15 but for $\gamma = 1.25$, $Re = 3050$, $Re - Re_{cr} \approx 179$, $\epsilon^2 \approx 3 \times 10^{-4}$.

so that in this case a noticeably larger supercriticality is necessary for the appearance of the oscillating bubble. Unlike the previous cases the oscillating bubble appears in the upper but not in the lower part of the flow (figure 19, $Re = 3600$).

To obtain a similar effect for $\gamma < 1$ larger supercriticalities are required, but since the formal asymptotic expansion (17) is not valid for larger supercriticalities such results cannot be obtained within the present framework.

The appearance of the oscillating separation bubble in flows with relatively small aspect ratio ($\gamma \leqslant 1.75$) takes place in the region of parameters where the stationary solution of the problem (below the critical Reynolds number as well as above it) does not predict a separation vortex bubble. The oscillating separation bubble appears as a result of the continuously developing oscillatory instability when the supercriticality is sufficiently large. Since the phenomenon as a whole is very similar to vortex breakdown in stationary flows it may be interpreted as 'oscillatory vortex breakdown'. It should be noticed that a separation bubble was reported by Lugt & Haussling (1973) for the almost rigid-body rotation of a counter-rotating disk–cylinder system with aspect ratio 1. This bubble occurred only temporarily and vanished when the steady state was reached. It is possible that this damped vortex breakdown is caused by an oscillatory perturbation mode.

4.4. *Straightforward simulation of slightly supercritical flows*

A numerical solution of the unsteady governing equations (1)–(5) was carried out to estimate the upper bound of the supercriticality below which the asymptotic expansions

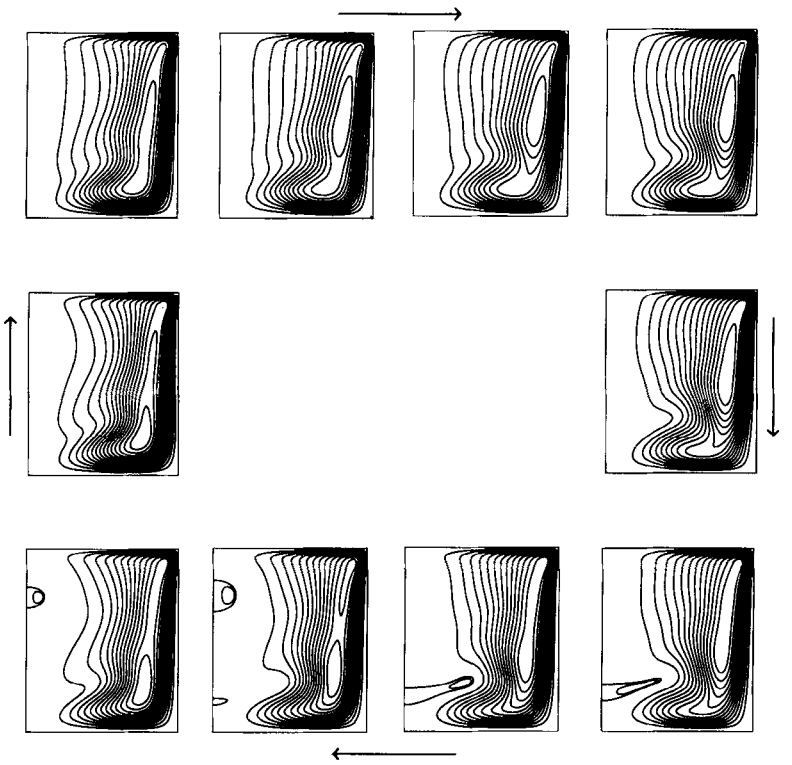

FIGURE 18. As figure 15 but for $\gamma = 1.25$, $Re = 3100$, $Re - Re_{cr} \approx 229$. $\epsilon^2 \approx 4 \times 10^{-4}$.

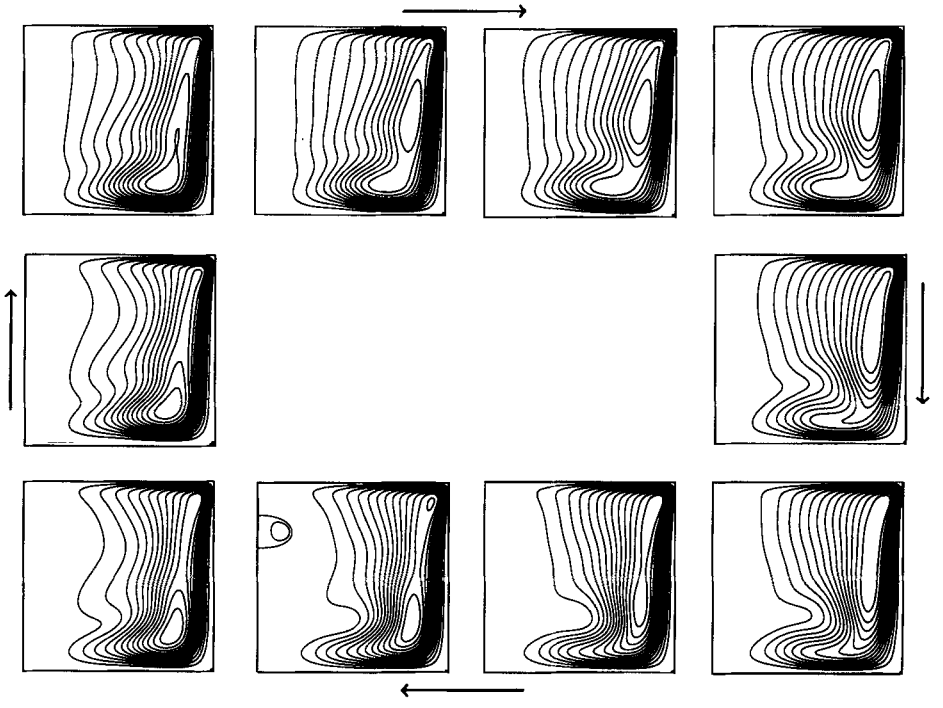

FIGURE 19. As figure 15 but for $\gamma = 1$, $Re = 3600$, $Re - Re_{cr} \approx 449$, $\epsilon^2 \approx 2 \times 10^{-4}$.

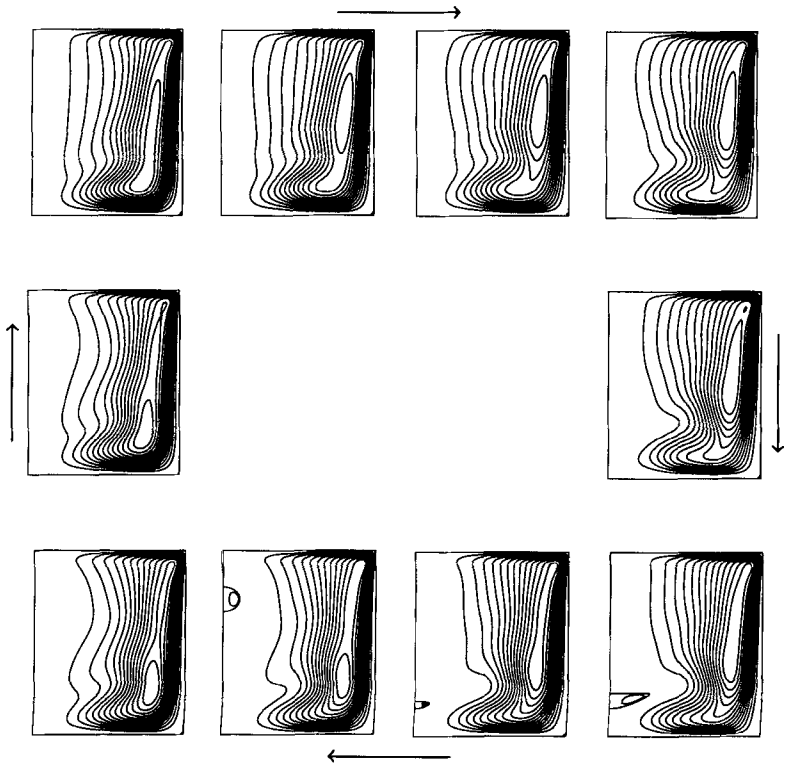

FIGURE 20. As figure 15 but for $\gamma = 1.25$, $Re = 3100$. Calculation with the finite volume method using 150×150 stretched grid.

(17) provide an approximation of the limit cycle which may be compared with the solution of the complete problem. The numerical solution was carried out using the finite volume method based on the SIMPLE algorithm (Patankar & Spalding 1972) and three levels approximation of the time derivative (Janssen, Henkes & Hoogendoorn 1993). The same stretching of the grid as in Tsitverblit (1993) was used.

It was found that the frequency of oscillations is already correctly approximated on the 75×75 nodes grid (figure 12*b*). However, to obtain good agreement of the instantaneous streamlines calculated by two different numerical approaches a much finer grid is necessary. For example, in the case $\gamma = 2.5$, $Re = 2765$ considered by Lopez (1990) and Lopez & Perry (1992) the supercriticality $Re - Re_{cr}$ is about 59 and ϵ^2 in the expansion (17) is approximately 5×10^{-5}. A grid of 150×150 nodes was necessary to obtain a good agreement between oscillatory solutions (figure 15) even for such small supercriticality.

Further calculations with 150×150 grid nodes allowed the confirmation of the existence of the oscillating separation vortex bubble in the case $\gamma = 1.5$, $Re = 2800$ (figure 16). However for larger supercriticalities (like those illustrated in figures 17–19) it was found that the asymptotic expansion (17) overestimates the amplitude of the oscillations. On the other hand, patterns of the oscillatory flows similar to those plotted in figures 17–19 may be obtained for larger values of Re. Thus, in the case $\gamma = 1.25$, $Re = 3050$ there are two distinct separation bubbles in the asymptotic solution (figure 17) but only the lower separation bubble is observed in the solution obtained with the finite volume method. The upper separation bubble appears in the finite volume solution after increase of the Reynolds number up to $Re = 3100$ (figure 20), but the

amplitude of the oscillations is smaller than predicted by the asymptotic expansion (figure 18). It may be concluded that in this case the oscillatory flow still can be described as superposition of the stationary solution and the perturbation, but higher-order terms in the asymptotic expansion (17) become significant. Nevertheless, the direct numerical simulation performed confirms a qualitative conclusion about the existence of one (figures 16 and 19) or two (figures 17, 18 and 20) pulsating separation vortex bubbles in slightly supercritical flows for $\gamma \leqslant 1.75$ which was done on the basis of weakly nonlinear analysis of the Hopf bifurcation.

5. Concluding remarks

It is shown that the change of signs of the azimuthal vorticity η and the function $\Phi = (\partial/\partial z)(\Gamma^2/r^3)$ is a necessary, but not sufficient, condition for B-type vortex breakdown. The change in the signs of η and Φ is caused by the non-monotone axial distribution of the centrifugal force which is a consequence of the convection of azimuthal velocity and action of the Coriolis force. It is our argument that the local maximum of the centrifugal force is the main reason for the appearance of recirculation zones in a swirling flow. It is shown that the concave shape of the streamsurfaces of a confined swirling flow may be considered as an additional property of vortex breakdown.

The appearance and disappearance of the vortex breakdown in steady states of the confined swirling flow considered here are not connected with the stability of the flow. The same may be said about the appearance and the disappearance of the second and third separation bubbles. The vortex breakdown appears and develops as a continuous change of the meridional flow with the variation of the Reynolds number.

For aspect ratio $1 \leqslant \gamma \leqslant 3$ the transition from a steady to an oscillatory flow regime takes place as a result of an axisymmetric supercritical Hopf bifurcation, which is caused by three different perturbation modes that successively replace each other with the growth of the aspect ratio. The onset of the oscillatory instability is not caused by and is not connected with the existence of the vortex breakdown in the flow.

For $\gamma \geqslant 3$ the experimentally observed oscillatory instability cannot be described by the axisymmetric stability analysis. This instability is caused by asymmetric perturbations of an axisymmetric flow. It is unclear whether it is an instability of stationary or oscillatory axisymmetric flow.

The weakly nonlinear analysis of the numerically obtained axisymmetric Hopf bifurcation shows that the bifurcation is supercritical for all values of the aspect ratio considered. The asymptotic approximation of the supercritical oscillatory flow in the case $\gamma \leqslant 1.75$ showed that at a certain finite supercriticality the evolution of the oscillatory instability may result in an oscillatory vortex breakdown, i.e. one or two oscillating separation bubbles may arise as a result of the instability in cases when no separation bubble is observed in steady sub- and supercritical states. This conclusion was proven by the direct numerical simulation of slightly supercritical flows.

This research was supported by the Center for Absorption in Science, Ministry of Immigrant Absorption, State of Israel (to A. Gelfgat), and by the Y. Winograd Chair of Fluid Mechanics and Heat Transfer at Technion.

Appendix

The convergence of the stationary solutions is presented in table 1 for the case $\gamma = 2.5$, $Re = 2000$ in terms of the following flow features: the value and location of the maximum and minimum of the stream function and the azimuthal vorticity – $\psi_{max}(r_{max}, z_{max})$ and $\psi_{min}(r_{min}, z_{min})$; $\eta_{max}(r_{max}, z_{max})$ and $\eta_{min}(r_{min}, z_{min})$; the value and location of the maximum value of the z- and φ-components of velocity at the cross-section $z = \gamma/2 - v_{max}(r_{max}, z = \gamma/2)$ and $w_{max}(r_{max}, z = \gamma/2)$; the value and location of the maximum of the r-component of velocity at the cross-section $r = 0.5 - u_{max}(r = 0.5, z_{max})$. In all the calculations the values of K_r and K_z were taken as $K_r = 100$ and $K_z = 30$. With $K_r = 100$ the approximation of the boundary condition $\Omega(r, z = \gamma) = r$ in the interval $0 \leqslant r \leqslant 0.999$ is of $O(10^{-5})$. The value $K_z = 30$ provides $Q_i = 0$ in (14) corresponding to d_{ij} for all $M_z \leqslant 30$.

The test calculations were carried out with the number of basis functions in the series (6) $N_r \times N_z = M_r \times M_z$ varying from 22×22 to 38×38. To verify the results obtained the steady problem was solved numerically by a specially developed second-order finite volume method using staggered grids with 60×60, 100×100, 200×200 and 300×300 nodes. To condense nodes near the boundaries we used the same stretching as Tsitverblit (1993). The corresponding results are shown in table 1.

The comparison of the steady solutions obtained with the Galerkin and the finite volume methods shows that 26×26 basis function suffice to yield a reasonable result. The steady solution converges rapidly with the increase of the number of Galerkin modes. The steady solution obtained with 38×38 basis functions is in good agreement with the solution obtained on the 300×300 grid. All the parameters, except the values of ψ_{min}, coincide at least up to the second digit. The values of ψ_{min} are very small and sensitive to discretization, such that even the result obtained with 300×300 nodes cannot be considered as accurate enough.

The convergence of critical Reynolds numbers and critical frequencies for $\gamma = 1.5$, 2.5, and 3.25 is shown in table 2 for numbers of the basis functions increasing from 24×24 to 38×38. It is seen from the table that the stability analysis for larger values of the aspect ratio requires larger numbers of Galerkin modes. Thus, the value of Re_{cr} in the case $\gamma = 1.5$ may be obtained with four correct digits using 26×26 basis functions, while in the case $\gamma = 3.25$ the second correct digit may be obtained only with 28×28 basis functions. The convergence of ω_{cr} is much faster, such that in all cases three correct digits of ω_{cr} are obtained with 24×24 basis functions. The calculated values of Re_{cr} and ω_{cr} are compared with the experimental results of Escudier (1984) in figure 12(*a*) and with the independent calculations in figure 12(*b*). The convergence of the calculated Re_{cr} and ω_{cr} is illustrated in figure 12(*c*).

The parameters μ and τ of the expansions (17) cannot be compared directly because they depend on the norm of the dominant eigenvector. For comparison of the weakly nonlinear expansions of the limit cycle obtained with different number of basis functions these parameters were scaled by the coefficient β in the expansion of the Floquet exponent (24). The convergence of the parameters μ and τ is determined mainly by the convergence of the derivative of the dominant eigenvalue and by the convergence of the corresponding left and right eigenvectors (equations (18)–(23)). It is seen from table 2 that not more than two correct digits in the ratios μ/β and τ/β could be obtained with the numbers of basis functions used.

The comparison of the instantaneous streamlines of a supercritical flow with the results of the direct numerical simulation is shown in figures 15 and 16. To verify the prediction of asymptotic expansion (17) we also tried to calculate the streaklines of the

	Galerkin method					Finite volume method			
	22×22 functions	26×26 functions	30×30 functions	34×34 functions	38×38 functions	60×60 stretched grid	100×100 stretched grid	200×200 stretched grid	300×300 stretched grid
ψ_{max}	0.007723	0.007665	0.007646	0.007651	0.007648	0.007689	0.007667	0.007653	0.007649
r_{max}	0.763	0.752	0.761	0.757	0.756	0.767	0.759	0.753	0.761
z_{max}	1.863	1.775	1.838	1.807	1.801	1.859	1.826	1.791	1.823
$\psi^1_{min} \times 10^{-5}$	−0.6252	−0.6953	−0.7424	−0.7478	−0.7489	−0.1564	−0.5304	−0.6989	−0.7291
r_{min}	0.0825	0.0847	0.0857	0.0858	0.0859	0.0563	0.0807	0.0832	0.0841
z_{min}	0.703	0.696	0.695	0.695	0.696	0.641	0.674	0.690	0.695
$\psi^2_{min} \times 10^{-6}$	−0.5240	−0.5220	−0.5434	−0.5568	−0.5526	−0.6108	−0.6034	−0.5570	−0.5642
r_{min}	0.0483	0.0478	0.0485	0.0487	0.0486	0.0473	0.0495	0.0485	0.0482
z_{min}	1.446	1.447	1.457	1.455	1.454	1.393	1.423	1.445	1.453
η_{max}	0.4847	0.4620	0.4663	0.4649	0.4637	0.4864	0.4721	0.4664	0.4653
r_{max}	0.228	0.253	0.239	0.255	0.248	0.233	0.241	0.247	0.244
z_{max}	0.238	0.270	0.272	0.271	0.268	0.258	0.261	0.269	0.272
η_{min}	−0.3812	−0.3974	−0.4033	−0.4026	−0.4016	−0.3679	−0.3907	−0.3959	−0.3993
r_{min}	0.194	0.196	0.196	0.196	0.196	0.211	0.201	0.206	0.195
z_{min}	0.652	0.641	0.640	0.637	0.638	0.642	0.638	0.653	0.634
$U_{max}(r = 0.5)$	0.09322	0.09246	0.09247	0.09252	0.09254	0.09049	0.09260	0.09261	0.09252
z_{max}	2.479	2.479	2.479	2.479	2.479	2.485	2.478	2.480	2.478
$V_{max}(z = \gamma/2)$	0.1104	0.1098	0.1093	0.1091	0.1091	0.1114	0.1099	0.1092	0.1091
r_{max}	0.762	0.762	0.762	0.764	0.761	0.767	0.759	0.764	0.763
$W_{max}(z = \gamma/2)$	0.04581	0.04593	0.04591	0.04591	0.04592	0.04610	0.04600	0.04593	0.045925
r_{max}	0.419	0.417	0.418	0.417	0.417	0.414	0.414	0.413	0.419

TABLE 1. Convergence study for steady state solutions ($\gamma = 2.5$; $Re = 2000$)

Aspect ratio	Parameter	24×24	26×26	28×28	30×30	32×32	34×34	36×36	38×38
$\gamma=1.5$	Re_{cr}	2725	2724	2724	2724	2724	2724	2724	2724
	ω_{cr}	0.236751	0.236754	0.236749	0.236748	0.236749	0.236752	0.236754	0.236753
	$\mu/\beta\times10^{-4}$	−2.605	−2.604	−2.600	−2.601	−2.603	−2.603	−2.602	−2.604
	τ/β	0.288	0.294	0.295	0.291	0.293	0.292	0.297	0.292
$\gamma=2.5$	Re_{cr}	2703	2706	2706	2705	2706	2706	2706	2706
	ω_{cr}	0.17234	0.17241	0.17240	0.172425	0.172452	0.17246	0.17245	0.17245
	$\mu/\beta\times10^{-4}$	−5.24	−5.13	−5.19	−5.20	−5.22	−5.25	−5.21	−5.23
	τ/β	1.74	1.94	1.93	1.87	1.87	1.89	1.85	1.87
$\gamma=3.25$	Re_{cr}	3430	3268	3209	3204	3198	3196	3198	3200
	ω_{cr}	0.1476	0.1477	0.1483	0.1486	0.1486	0.1487	0.1487	0.1487
	$\mu/\beta\times10^{-4}$	−4.85	−4.58	−3.91	−3.86	−3.84	−3.81	−3.80	−3.81
	τ/β	1.75	1.92	1.83	1.90	1.93	1.86	1.87	1.85

TABLE 2. Convergence study for the critical parameters and parameters of the limit cycle

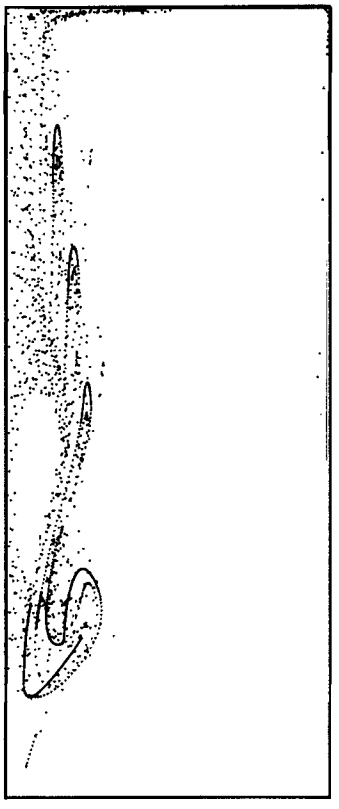

FIGURE 21. Unsteady streaklines calculated for $\gamma = 2.5$, $Re = 2765$.

supercritical flow for the same parameters as in the work of Lopez & Perry (1992), $\gamma = 2.5$, $Re = 2765$. The result is shown in figure 21. It should be noted that the asymptotic expansion (17) may contain a rather large residual. Because of this it should not be used for integration over very long periods of time, since at each time step numerical error may accumulate. Nevertheless, integrating over a time corresponding to several tens of periods (which is not very large) allowed us to obtain a picture of streaklines (figure 21) with the main features very similar to those obtained by Lopez & Perry (1992).

REFERENCES

ARKADYEV, A., BAR-YOSEPH, P., SOLAN, A. & ROESNER, K. G. 1993 Thermal effects on axisymmetric vortex breakdown in a spherical gap. *Phys. Fluids* A **5**, 1211–1223.

BAR-YOSEPH, P. 1994 On multiple flow patterns and vortex breakdown phenomena in confined rotating flows. *Comput. Fluid Dyn. J.* **3**, 273–292.

BAR-YOSEPH, P. & KRYZHANOVSKI, YU. 1995 On the validity of power law models in the prediction of vortex breakdown phenomena. *6th Intl Symp. on Computational Fluid Dynamics* (ed. M. Hafez), *Lake Tahoe, Nevada, September 4–8*, pp. 29–34; *Comput. Fluid Dyn.* (to appear).

BAR-YOSEPH, P., ROESNER, K. G. & SOLAN, A. 1992 Vortex breakdown in the polar region between rotating spheres. *Phys. Fluids* A **4**, 1677–1686.

BROWN, G. L. & LOPEZ, J. M. 1990 Axisymmetric vortex breakdown. Part 2. Physical mechanisms. *J. Fluid Mech.* **221**, 533–576.

CHRISTENSEN, E. A., SØRENSEN, J. N., BRØNS, M. & CHRISTIANSEN P. L. 1993 Low-dimensional representation of early transition in rotating fluid flow. *Theor. Comput. Fluid Dyn.* **5**, 259–267.

DAUBE, O. 1992 Resolution of the 2D Navier–Stokes equations in velocity-vorticity form by means of an influence matrix technique. *J. Comput. Phys.* **103**, 402–414.

DAUBE, O. & SØRENSEN, J. N. 1989 Simulation numérique de l'écoulement périodique axisymmétrique dans une cavité cylindrique. *C. R. Acad. Sci. Paris* **308**, 463–469.

DAVIDSON, P. A. 1989 The interaction between swirling and recirculating velocity components in unsteady, inviscid flow. *J. Fluid Mech.* **209**, 35–55.

DELERY, J. M. 1994 Aspects of vortex breakdown. *Prog. Aerosp. Sci.* **30**, 1–59.

ESCUDIER, M. P. 1984 Observation of the flow produced in a cylindrical container by a rotating endwall. *Exps. Fluids* **2**, 189–196.

ESCUDIER, M. P. 1988 Vortex breakdown: observations and explanations. *Proc. Aerosp. Sci.* **25**, pp. 189–229.

GELFGAT, A., BAR-YOSEPH, P. & SOLAN, A. 1995 Numerical investigation of a confined swirling flow in a cylinder with rotating top and bottom by the Galerkin spectral method. *6th Intl Symp. on Computational Fluid Dynamics* (ed. M. Hafez), *Lake Tahoe, Nevada, September 4–8*, pp. 355–360.

GELFGAT, A. YU. & TANASAWA, I. 1993 Systems of basis functions for calculation of three-dimensional fluid flows in cylindrical containers with the Galerkin spectral method. *Proc. Inst. Indust. Sci., Univ. Tokyo* **45** (8), 60–63.

GELFGAT, A. YU. & TANASAWA, I. 1994 Numerical analysis of oscillatory instability of buoyancy convection with the Galerkin spectral method. *Numer. Heat Transfer* A: *Applications* **25**, 627–648.

HASSARD, B. D., KAZARINOFF, N. D. & WAN, Y.-H. 1981 *Theory and Applications of Hopf Bifurcation*. London Math. Soc. Lecture Note Series, vol. 41.

HOPF, E. 1942 Abzweigung einer Periodischen Losung von Einer Stationaren Losung eines Differentialsystems. *Ber. Verh. Sachs. Acad. Wiss. Leipsig Math.-Nat.* **94**, 3–22.

HOPFINGER, E. J. & LINDEN, P. F. 1990 The effect of background rotation on fluid motions. *J. Fluid Mech.* **211**, 417–435.

JANSSEN, R. J. A., HENKES, R. A. W. M., HOOGENDOORN, C. J. 1993 Transition to time-periodicity of a natural convection flow in a 3D differentially heated cavity. *Intl J. Heat Mass Transfer* **36**, 2927–2940.

LOPEZ, J. M. 1990 Axisymmetric vortex breakdown. Part 1. Confined swirling flow. *J. Fluid Mech.* **221**, 533–552.

LOPEZ, J. M. 1994 On the bifurcation structure of axisymmetric vortex breakdown in a constricted pipe. *Phys. Fluids* **6**, 3683–3693.

LOPEZ, J. M. & PERRY, A. D. 1992 Axisymmetric vortex breakdown. Part 3. Onset of periodic flow and chaotic advection. *J. Fluid Mech.* **234**, 449–471.

LUGT, H. J. & ABBOUD, M. 1987 Axisymmetric vortex breakdown with and without temperature effects in a container with a rotating lid. *J. Fluid Mech.* **179**, 179–200.

LUGT, H. J. & HAUSSLING, H. J. 1973 Development of flow circulation in a rotating tank. *Acta Mechanica* **18**, 255–272.

NEITZEL, G. P. 1988 Streak-line motion during steady and unsteady axisymmetric vortex breakdown. *Phys. Fluids* **31**, 958–960.

PATANKAR, S. V. & SPALDING, D. B. 1972 A calculation procedure for heat, mass and momentum transfer in three-dimensional parabolic flows. *Intl J. Heat Mass Transfer* **15**, 1787–1806.

ROESNER, K. G. 1990 Recirculation zones in a cylinder with rotating lid. In *Topological Fluid Mechanics* (ed. H. K. Moffat & A. Tsinober), pp. 699–708. Cambridge University Press.

SØRENSEN, J. N. & DAUBE, O. 1989 Direct simulation of flow structures initiated by a rotating cover in a cylindrical vessel. In *Advances in Turbulence* (ed. H. H. Fernholz & H. E. Fielder), pp. 383–390. Springer.

TSITVERBLIT, N. 1993 Vortex breakdown in a cylindrical container in the light of continuation of a steady solution. *Fluid Dyn. Res.* **11**, 19–35.

TSITVERBLIT, N. & KIT, E. 1994 On the onset of nonsteadiness in the flows with vortex breakdown in a cylindrical container. *Proc. IUTAM Symp on Nonlinear Instability of Nonparallel Flows* (ed. S. P. Lin, W. R. C. Phillips & D. T. Valentine), pp. 310–319. Springer.

VOGEL, H. U. 1975 Rückströmungsblasen in Drallströmungen. In *Festschrift zum 50-jährigen Bestehen des MPI für Strömungsforschung*, pp. 263–272. Hubert, Göttingen.